

*Aki Kärnä*

MODELLING OF SUPERSONIC  
TOP LANCE AND THE HEAT-UP  
STAGE OF THE CAS-OB PROCESS

UNIVERSITY OF OULU GRADUATE SCHOOL;  
UNIVERSITY OF OULU,  
FACULTY OF TECHNOLOGY





ACTA UNIVERSITATIS OULUENSIS  
C Technica 685

**AKI KÄRNÄ**

**MODELLING OF SUPERSONIC TOP  
LANCE AND THE HEAT-UP STAGE  
OF THE CAS-OB PROCESS**

Academic dissertation to be presented with the assent of the Doctoral Training Committee of Technology and Natural Sciences of the University of Oulu for public defence in Kaljusensali (KTK112), Linnanmaa, on 23 November 2018, at 12 noon

UNIVERSITY OF OULU, OULU 2018

Copyright © 2018  
Acta Univ. Oul. C 685, 2018

Supervised by  
Professor Timo Fabritius  
Associate Professor Mika Järvinen

Reviewed by  
Assistant Professor Mikael Ersson  
Docent Mikko Helle

Opponent  
Associate Professor Ari Jokilaakso

ISBN 978-952-62-2105-2 (Paperback)  
ISBN 978-952-62-2106-9 (PDF)

ISSN 0355-3213 (Printed)  
ISSN 1796-2226 (Online)

Cover Design  
Raimo Ahonen

JUVENES PRINT  
TAMPERE 2018

## **Kärnä, Aki, Modelling of supersonic top lance and the heat-up stage of the CAS-OB process.**

University of Oulu Graduate School; University of Oulu, Faculty of Technology

*Acta Univ. Oul. C 685, 2018*

University of Oulu, P.O. Box 8000, FI-90014 University of Oulu, Finland

### *Abstract*

The CAS-OB (composition adjustment by sealed argon bubbling - oxygen blowing) process is used in secondary steelmaking to adjust the composition and temperature of the steel melt. The steel melt can be heated by oxidizing aluminium in process which feeds aluminium particles and oxygen to the melt surface. Oxygen is fed by a top lance, which is an important part of many metallurgical processes and is typically used to deliver oxygen to steel melt surface by supersonic blowing.

Because observing and measuring the metallurgical processes is challenging due to the high temperature, numerical models predicting the processes are especially important. In this thesis, both top lances and the heat-up stage of the CAS-OB process were studied, and numerical models were constructed.

CFD (computational fluid dynamics) were used to study top lances. A turbulence model was adjusted for supersonic flows with experimental data from literature. The CAS-OB process model involves chemical reactions and fluid flows. In order to keep the computation times reasonable, a full fluid flow calculation is not included in the model but is calculated in advance. Heat and mass transfer correlations are calculated with CFD, and the results are then used in the process simulation model. Chemical reactions are calculated based on the law of mass action and thermodynamics.

The results were validated with industrial measurements. The CAS-OB heat-up stage model can be used in its current state in process development, and in the future for online control of the process. The CFD model for the top lance can be applied to a lance in any other process.

*Keywords:* CAS-OB, CFD, chemical reactions, numerical modelling, top lance



## **Kärnä, Aki, Yliäänilanssin ja CAS-OB-prosessin lämmitysvaiheen mallinnus.**

Oulun yliopiston tutkijakoulu; Oulun yliopisto, Teknillinen tiedekunta

*Acta Univ. Oul. C 685, 2018*

Oulun yliopisto, PL 8000, 90014 Oulun yliopisto

### ***Tiivistelmä***

CAS-OB-prosessia (composition adjustment by sealed argon bubbling - oxygen blowing) käytetään teräksen valmistuksessa sulan teräksen koostumuksen ja lämpötilan säätämiseen. Terässulaa voidaan tarvittaessa lämmittää syöttämällä alumiinikappaleita ja happea sulan pinnalle. Hapen syöttö tapahtuu yliäänilanssilla, jota käytetään monissa metallurgisissa prosesseissa, yleensä toimittamaan happea sulan pinnalle yliäänisellä puhalluksella.

Metallurgisten prosessien havainnointi ja mittaaminen ovat haastavia korkeiden lämpötilojen vuoksi, joten numeeriset mallit ovat erityisen tärkeitä prosessien ennustamisessa. Tässä työssä on tutkittu yliäänilansseja ja CAS-OB-prosessin lämmitysvaihetta ja luotu niille numeeriset mallit.

Yliäänilanssien tutkimiseen käytettiin numeerista virtauslaskentaa (CFD, computational fluid dynamics). Lanssien mallinnusta varten olemassa olevaa turbulenssimallia muokattiin paremmin yliäänivirtausta kuvaavaksi kirjallisuudesta löytyvän mittaustiedon perusteella. CAS-OB-prosessimallissa huomioidaan virtaus ja kemialliset reaktiot. Koska laskenta-ajat haluttiin pitää käytännöllisinä, virtauslaskentaa ei suoriteta mallissa, vaan se tehdään etukäteen. Aineen- ja lämmönsiirtokertoimet lasketaan CFD-laskennalla, ja tuloksia käytetään prosessimallissa. Kemialliset reaktiot lasketaan perustuen massavaikutuksen lakiin ja termodynamiikkaan.

CAS-OB-mallin tulokset on validoitu terästehtaalla tehtyjen kokeiden perusteella. Mallia voidaan käyttää nykyisessä muodossaan prosessin kehityksessä ja tulevaisuudessa myös prosessin ohjauksessa. Yliäänilanssin CFD-mallia voidaan soveltaa myös muihin metallurgisiin prosesseihin.

*Asiasanat:* CAS-OB, kemialliset reaktiot, numeerinen mallinnus, virtauslaskenta, yliäänilanssi



## Acknowledgements

The research for this thesis was conducted in 2011-2018 at the Process Metallurgy Research Unit at the University of Oulu. The work has been funded by the Finnish Funding Agency for Technology and Innovation (TEKES) in the Energy and Lifecycle Efficient Metal Processes (ELEMET) and System Integrated Metal Production (SIMP) programmes, the Academy of Finland projects 258319 and 26495, as well as the Jenny and Antti Wihuri Foundation and Tauno Tönning foundation.

I would like to thank my supervisors Professor Timo Fabritius and Associate Professor Mika Järvinen for their guidance and encouragement. Special thanks go to my closest co-workers Dr. Petri Sulasalmi and Dr. Ville-Valtteri Visuri. I also wish to thank co-authors Docent Eetu-Pekka Heikkinen, Docent Cataldo De Blasio and Katja Pääskylä.

I would like to acknowledge Seppo Ollila from SSAB Europe Oy for arranging the industrial measurements and providing information on the CAS-OB and Pentti Kupari from Outokumpu Stainless Oy for his cooperation in lance studies.

Pre-examiners Associate Professor Mikael Ersson and Docent Mikko Helle are acknowledged for their valuable comments concerning this thesis.

Finally, I would like to thank all of you who were involved in all other ways with this project.



## Abbreviations

AOD	Argon oxygen decarburisation
BOF	Basic oxygen furnace
CAS	Composition adjustment by sealed argon bubbling
CAS-OB	Composition adjustment by sealed argon bubbling - oxygen blowing
CFD	Computational fluid dynamics
DNS	Direct numerical simulation
DPM	Discrete phase model
HALT	Heating advanced ladle treatment
IR-UT	Injection refining up-temperature
LES	Large eddy simulation
LD	Linz and Donawitz
MAE	Mean absolute error
MOC	Method of characteristics
NASA	National Aeronautics and Space Administration
NIST	National Institute of Standards and Technology
NTP	Normal temperature and pressure
OES	Optical emission spectroscopy
POSCO	Pohang iron and steel company
RANS	Reynold averaged Navier-Stokes
REH	Reactive element heating
RH-OB	Ruhrstahl Heraeus - oxygen blowing
RSM	Reynolds stress model
SA	Spalart-Allmaras
SAS	Scale-adaptive simulation
SST	Shear stress transport
UDF	User defined function
UIP	Unified interaction parameter
VD-OB	Vacuum degasser - oxygen blowing
VOF	Volume of fluid
XRF	X-ray fluorescence spectroscopy

## Symbols

$A_{Al}$	Surface area of pure aluminium layer [m <sup>2</sup> ]
$A_{Al,S}$	Surface area of the solid aluminium particles in contact with the steel melt [m <sup>2</sup> ]
$A_{B1}$	Area of the bell interior surface [m <sup>2</sup> ]
$A_{B1,sub}$	Area of the bell interior surface submerged in the steel melt [m <sup>2</sup> ]
$A_{B1,o}$	Surface area between occupied surface layer and the bell [m <sup>2</sup> ]
$A_{B2}$	Surface area between the slag layer and the bell [m <sup>2</sup> ]
$A_{B2,sub}$	Area of the bell bottom surface [m <sup>2</sup> ]
$A_{B3}$	Surface area between the bell brick layer and the steel mantle [m <sup>2</sup> ]
$A_{B4}$	Surface area of bell exterior [m <sup>2</sup> ]
$A_d$	Surface area of the steel droplets [m <sup>2</sup> ]
$A_e$	Nozzle exit area [m <sup>2</sup> ]
$A_f$	Surface area of the jet impact cavity, the free surface [m <sup>2</sup> ]
$A_{L1}$	Surface area between the steel melt and the ladle [m <sup>2</sup> ]
$A_{L2}$	Surface area of the ladle brick layer [m <sup>2</sup> ]
$A_{L3}$	Surface area in between the ladle brick layer and the steel mantle [m <sup>2</sup> ]
$A_{L4}$	Area of the ladle exterior surface [m <sup>2</sup> ]
$A_{L,rad}$	Exposed surface area of the ladle above the melt level [m <sup>2</sup> ]
$A_o$	Surface area of the occupied surface [m <sup>2</sup> ]
$A_{S1}$	Surface area of the slag layer outside the bell [m <sup>2</sup> ]
$A_t$	Nozzle throat area [m <sup>2</sup> ]
$a_i$	Activity of species $i$
$B(\dot{m}_{g,f}, i)$	Stefan flow of component $i$ in gas [kg/(m <sup>2</sup> ·s)]
$B(\dot{m}_{g,Al}, i)$	Stefan flow of component $i$ in gas [kg/(m <sup>2</sup> ·s)]
$B(\dot{m}_l, i)$	Stefan flow of component $i$ in steel melt [kg/(m <sup>2</sup> ·s)]
$B(\dot{m}_{l,d}, i)$	Stefan flow of component $i$ in steel droplets [kg/(m <sup>2</sup> ·s)]
$C_1$	Turbulence model coefficient
$C_2$	Turbulence model coefficient
$C_3$	Turbulence model coefficient
$C_D$	Drag coefficient
$C_\mu$	Turbulent viscosity coefficient
$c$	Speed of sound [m/s]
$c_p$	Specific heat at constant pressure [J/(kg·K)]

$c_v$	Specific heat in constant volume [J/(kg·K)]
$D_i$	Diffusion coefficient [ $\text{m}^2/\text{s}$ ]
$d_a$	Thickness of attached material inside the bell [m]
$d_d$	Droplet diameter [m]
$d_f$	Jet cavity diameter [m]
$dx_{Ls}$	Steel shell thickness [m]
$dx_{Lb}$	Ladle brick layer thickness [m]
$dx_{Bb}$	Bell brick layer thickness [m]
$dx_{Bs}$	Bell steel shell thickness [m]
$E$	Equilibrium number
$E_{bi}$	Black body radiation from surface $i$ [ $\text{W}/\text{m}^2$ ]
$F_{ij}$	View factor
$\Delta G_c$	Conversion factor between the regular solution and the real solution [J/mol]
$\Delta G^\circ$	Gibbs standard free energy [J/mol]
$\Delta G_i^\circ$	Gibbs standard free energy change of reaction $i$ [J/mol]
$G_b$	Generation of turbulence kinetic energy by buoyancy [ $\text{m}^2/\text{s}^2$ ]
$G_k$	Generation of turbulence kinetic energy by mean velocity gradients [ $\text{m}^2/\text{s}^2$ ]
$G_\omega$	Generation of specific dissipation rate [1/s]
$g$	Gravitational acceleration [ $\text{m}/\text{s}^2$ ]
$H$	Height [m]
$H^\circ$	Standard enthalpy [J/mol]
$H_{B2}$	Height of the bell brick layer [m]
$H_f$	Height of the jet cavity [m]
$H_{slag}$	Height of the slag layer outside the bell [m]
$H_s$	Height of the slag layer inside the bell [m]
$h_{Al,S}$	Mass transfer coefficient for the solid aluminium particles in steel [m/s]
$h_{Al,L}$	Mass transfer coefficient of liquid aluminium [m/s]
$h_i$	Mass transfer coefficient of component $i$ in steel [m/s]
$h_{i,d}$	Mass transfer coefficient of component $i$ in steel droplets [m/s]
$h_{i,f}$	Mass transfer coefficient of component $i$ in gas at free surface [m/s]
$h_{i,Al}$	Mass transfer coefficient of component $i$ in gas at aluminium surface [m/s]
$\Delta h_k$	Specific enthalpy change of reaction $k$ [J/kg]

$J_i$	Radiosity of surface $i$ [ $\text{W}/\text{m}^2$ ]
$K$	Equilibrium constant
$k$	Turbulence kinetic energy [ $\text{m}^2/\text{s}^2$ ]
$k_a$	Apparent rate constant
$k_b$	Backward reaction rate coefficient [ $\text{kg}/(\text{m}^2 \cdot \text{s})$ ]
$k_c$	Chemical rate constant
$k_f$	Forward reaction rate coefficient [ $\text{kg}/(\text{m}^2 \cdot \text{s})$ ]
$l_m$	Latent heat of melting [ $\text{J}/\text{kg}$ ]
$M$	Molar mass [ $\text{kg}/\text{mol}$ ]
$\dot{M}$	Dimensionless momentum flux
$Ma$	Mach number
$\dot{m}$	Total mass flow rate [ $\text{kg}/\text{s}$ ]
$m_{Al,S}$	Mass of solid aluminium [ $\text{kg}$ ]
$m_D$	Mass of steel droplets [ $\text{kg}$ ]
$N_B$	Blowing number
$Nu$	Nusselt number
$p$	Pressure [ $\text{Pa}$ ]
$p_0$	Inlet pressure [ $\text{Pa}$ ]
$p_a$	Ambient pressure [ $\text{Pa}$ ]
$p_e$	Exit pressure [ $\text{Pa}$ ]
$Pr$	Prandtl number
$Q$	Reaction quotient
$q$	Heat flux [ $\text{W}/(\text{m}^2 \cdot \text{s})$ ]
$R$	Universal gas constant [ $\text{J}/(\text{mol} \cdot \text{K})$ ]
$R$	Reaction rate [ $\text{kg}/(\text{m}^2 \cdot \text{s})$ ]
$R_d$	Steel droplet generation rate [ $\text{kg}/\text{s}$ ]
$R_{melt}$	Melting rate of solid aluminium [ $\text{kg}/\text{s}$ ]
$R_g$	Specific gas constant [ $\text{J}/(\text{kg} \cdot \text{K})$ ]
$Re$	Reynolds number
$S^\circ$	Standard entropy [ $\text{J}/(\text{mol} \cdot \text{K})$ ]
$S_m$	Mass source term [ $\text{kg}$ ]
$Sh$	Sherwood number
$T$	Temperature [ $\text{K}$ ]
$T_{Al,in}$	Aluminium feed temperature [ $\text{K}$ ]
$T_{Al,melt}$	Aluminium melting temperature [ $\text{K}$ ]

$T_{Ar,in}$	Argon feed temperature [K]
$T_{atm}$	Ambient temperature [K]
$T_{B1}$	Temperature of the inner surface of the bell [K]
$T_{B2}$	Bell brick layer temperature [K]
$T_{B3}$	Temperature between the bell brick layer and the steel mantle [K]
$T_{B4}$	Temperature of the outer surface of the bell [K]
$T_f$	Temperature at the free surface [K]
$T_g$	Temperature in gas [K]
$T_{L1}$	Temperature of the inner surface of the ladle [K]
$T_{L2}$	Ladle brick layer temperature [K]
$T_{L3}$	Temperature between the ladle brick layer and the steel mantle [K]
$T_{B4}$	Temperature of the outer surface of the ladle [K]
$T_l$	Temperature of the steel melt [K]
$T_m$	Aluminium melting temperature [K]
$T_o$	Temperature at the occupied surface [K]
$T_{O_2,in}$	Oxygen feed temperature [K]
$T_{S1}$	Temperature at the bottom of the slag layer [K]
$T_{S2}$	Temperature at the top of the slag layer [K]
$u$	Velocity [m/s]
$\vec{v}_p$	Velocity of the dispersed phase [m/s]
$\vec{v}_q$	Velocity of the continuous phase [m/s]
$\dot{V}_g$	Volume flux [m <sup>3</sup> /s]
$X_{ij}$	Cation fraction
$x_i$	Mole fraction
$x$	Distance [m]
$Y_M$	Effect of compressibility on turbulence [m <sup>2</sup> /s <sup>2</sup> ]
$Y_V$	Destruction of kinematic turbulent viscosity [m <sup>2</sup> /s]
$Y_\omega$	Destruction of specific dissipation rate [1/s]
$y_i$	Mass fraction

### Greek symbols

$\alpha_{ij}$	Interaction energy [J]
$\alpha_{B1}$	Heat transfer coefficient between gas and the bell interior [W/(m <sup>2</sup> ·K)]
$\alpha_{B4}$	Heat transfer coefficient between air and the bell exterior [W/(m <sup>2</sup> ·K)]
$\alpha_d$	Heat transfer coefficient inside the steel droplets [W/(m <sup>2</sup> ·K)]

$\alpha_{g,f}$	Heat transfer coefficient between gas and the free surface [W/(m <sup>2</sup> ·K)]
$\alpha_{g,o}$	Heat transfer coefficient between gas and the occupied surface [W/(m <sup>2</sup> ·K)]
$\alpha_{LA}$	Heat transfer coefficient between air and the ladle exterior [W/(m <sup>2</sup> ·K)]
$\alpha_{i,L}$	Heat transfer coefficient between the steel melt and the ladle wall [W/(m <sup>2</sup> ·K)]
$\alpha_{i,f}$	Heat transfer coefficient between the steel melt and the free surface [W/(m <sup>2</sup> ·K)]
$\alpha_{i,o}$	Heat transfer coefficient between the steel melt and the occupied surface [W/(m <sup>2</sup> ·K)]
$\alpha_{i,S1}$	Heat transfer coefficient between the steel melt and the slag layer [W/(m <sup>2</sup> ·K)]
$\alpha_s$	Heat transfer coefficient in the slag layer [W/(m <sup>2</sup> ·K)]
$\alpha_p$	Volume fraction of the dispersed phase
$\alpha_q$	Volume fraction of the continuous phase
$\gamma$	Ratio of specific heats
$\gamma_i$	Activity coefficient of component $i$
$\varepsilon$	Turbulence dissipation rate [m <sup>2</sup> /s <sup>3</sup> ]
$\varepsilon_{ij}$	Interaction coefficient of species $i$ and $j$
$\eta$	Parameter
$\eta$	Heat transfer efficiency
$\lambda_e$	Effective heat conductivity [W/(m·K)]
$\lambda_s$	Heat conductivity of slag [W/(m·K)]
$\lambda_a$	Heat conductivity of the material attached to the bell interior [W/(m·K)]
$\lambda_{brick}$	Heat conductivity of the brick layer [W/(m·K)]
$\lambda_{steel}$	Heat conductivity of the steel mantle [W/(m·K)]
$\mu$	Dynamic viscosity [Pa·s]
$\mu_t$	Turbulent viscosity [Pa·s]
$\nu$	Kinematic viscosity [m <sup>2</sup> /s]
$\nu_A$	Stoichiometric coefficient of A
$\nu_A^*$	Mass-based stoichiometric coefficient of A
$\rho$	Density [kg/m <sup>3</sup> ]
$\rho_g$	Gas density [kg/m <sup>3</sup> ]
$\rho_l$	Melt density [kg/m <sup>3</sup> ]
$\sigma_k$	Turbulence model coefficient
$\sigma_\varepsilon$	Turbulence model coefficient

$\sigma_l$	Surface tension of melt [N/m]
$\bar{\tau}$	Stress tensor [N/m <sup>2</sup> ]
$\tau_d$	Droplet residence time [s]
$\tau_m$	Melting time [s]
$\phi$	Generic transport scalar
$\omega$	Specific dissipation rate [1/s]



## List of original publications

This doctoral dissertation is based on the following articles, which are referred to in the text by their Roman numerals (I–IV):

- I Kärnä, A., Järvinen, M., & Fabritius, T. (2013). Supersonic lance mass transfer modelling. *Materials Science Forum*, 762, 686-690.
- II Järvinen, M., Kärnä, A., Visuri, V.-V., Sulasalmi, P., Heikkinen, E.-P., Pääskylä, K., De Blasio, C., Ollila, S., & Fabritius, T. (2014). A novel approach for numerical modeling of the CAS-OB process: Process model for the heat-up stage. *ISIJ International*, 54(10), 2263-2272.
- III Kärnä, A., Järvinen, M. P., & Fabritius, T. (2015). CFD modeling of a supersonic top blown lance in a CAS-OB process – development of gas heat and mass transfer correlation. *Steel Research International*, 86(11), 1370–1378.
- IV Kärnä, A., Järvinen, M., Sulasalmi, P., Visuri, V.-V., Ollila, S., & Fabritius, T. (2018). An improved model for the heat-up stage of the CAS-OB process: Development and validation. *Steel Research International*, 89(10). doi: 10.1002/srin.201800141

In all papers the idea of the paper in question resulted from the collaboration of all authors. The research work was conducted by the author of this thesis in papers I, III and IV. In paper II the author of this thesis developed the supersonic lance heat and mass transfer correlation, which is essential part of the model, and took part in the validation data collecting and writing of the paper. Papers I, III and IV were written by the author of this thesis.



# Contents

Abstract

Tiivistelmä

Acknowledgements 7

Abbreviations 9

List of original publications 17

Contents 19

**1 Introduction 21**

1.1 Top lance ..... 21

1.2 The CAS-OB process ..... 21

1.3 Aims of this study ..... 23

1.4 Work outline ..... 25

**2 Literature section 27**

2.1 Supersonic lances ..... 27

2.2 Reaction modelling ..... 33

2.2.1 Chemical equilibrium model ..... 34

2.2.2 Model with explicit reaction rate descriptions ..... 35

2.2.3 Indirect model ..... 36

2.2.4 Models of the CAS-OB process ..... 39

**3 Methods 43**

3.1 CFD modelling ..... 43

3.1.1 Conservation equations ..... 44

3.1.2 Turbulence ..... 45

3.1.3 CFD models developed ..... 48

3.2 CAS-OB heating stage model ..... 55

3.2.1 Reaction system ..... 56

3.2.2 Mass transfer ..... 59

3.2.3 Radiation heat transfer ..... 61

3.2.4 Mass conservation ..... 61

3.2.5 Energy conservation ..... 64

3.3 Validation measurements ..... 68

<b>4</b>	<b>Results and discussion</b>	<b>69</b>
4.1	CFD results .....	69
4.1.1	Turbulence model tests .....	69
4.1.2	Supersonic lance .....	73
4.1.3	Lance heat and mass transfer coefficients .....	76
4.1.4	View factors .....	79
4.2	CAS-OB heating stage process model .....	81
4.2.1	Temperature .....	82
4.2.2	Chemical composition .....	83
<b>5</b>	<b>Conclusions</b>	<b>87</b>
	<b>References</b>	<b>89</b>
	<b>Original publications</b>	<b>97</b>

# 1 Introduction

## 1.1 Top lance

A top lance is a pipe used to blow oxygen into the melt surface from above. Usually the lance is water cooled and equipped with one or multiple de Laval nozzles, that produce a supersonic gas velocity.

The first supersonic lance jet was used in 1949 at Linz and Donawitz in Austria to refine molten iron (Deo & Boom, 1993, 26). Prior to that oxygen was delivered to melt via bottom blowing, directly into melt from the vessel bottom or wall. In 1952 the first commercial steel was produced by LD-process (Linz and Donawitz) (Kirkaldy & Ward, 1964, 152).

In steel converters, where the oxygen could be fed from the bottom of the vessel directly into the melt, the reasons for using a top lance are (Chatterjee, Marique, & Nilles, 1984):

- To achieve a simple, separate oxygen supply, which is not part of the converter.
- To create droplets and emulsions which enhance the reaction rate.
- To control the oxygen feed by altering the lance height.

The disadvantages of using a top lance include dust formation and high oxygen contents in the slag and metal bath. Top blowing is not efficient in bath mixing, unlike bottom blowing. Therefore, in many processes top and bottom blowing are used together. Most often the top lance is used in converter processes where significant amounts of oxygen gas are needed for carbon removal from the melt.

In secondary metallurgy, the top lance is used for chemical heating in degasser (VD-OB, RH-OB, RH-TOP) and ladle treatment processes (CAS-OB, HALT, IR-UT, REH) (Stolte, 2007).

## 1.2 The CAS-OB process

The CAS-OB process (composition adjustment by sealed argon bubbling - oxygen blowing) is a ladle treatment process developed by the Nippon Steel Corporation. In 1977 they first introduced the CAS process for alloying, and later it evolved into the CAS-OB process, including oxygen blowing for heating (Kusunoki et al., 2013). The

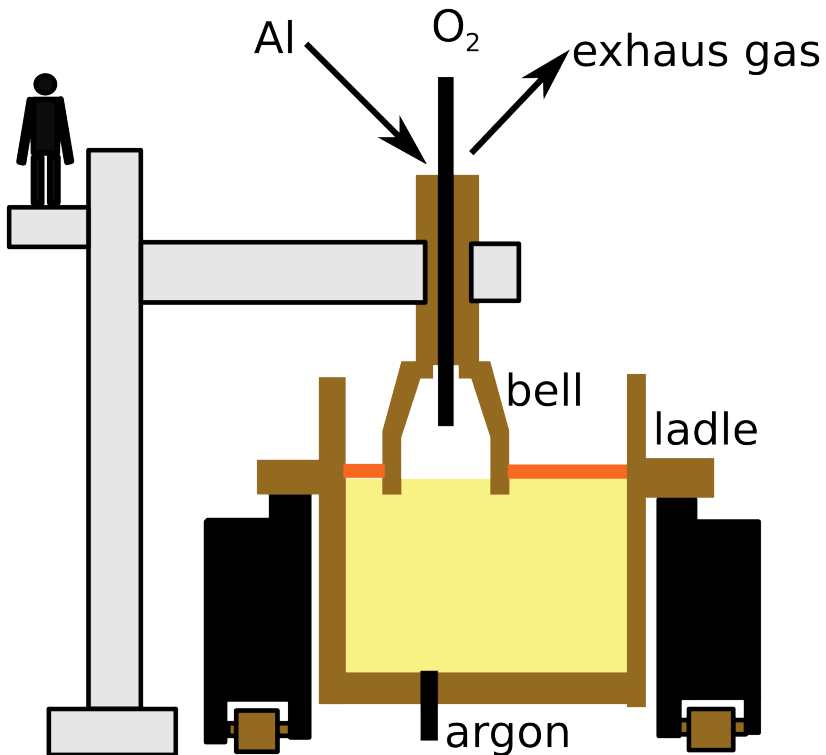


Fig. 1. CAS-OB device, drawn after Audebert, Gugliermi, Reboul, and Sauermann (1989).

process is used to adjust the steel composition and temperature. According to Ollila, Syrjänen, and Robey (2011) the main functions of the CAS-OB process are:

1. Homogenisation of the steel melt, composition and temperature.
2. Adjustment of the composition and temperature.
3. Improvement of the alloy yield.
4. Cleaning the steel.
5. Heating the steel.

An important part of CAS-OB is the bell or snorkel, which is used to create a sealed atmosphere at the melt surface. The ladle and the bell can be seen in Figure 1. Argon gas is fed through porous plugs in the bottom of the ladle, mainly for bath mixing. Bottom bubbling can be used to make an open eye in the slag layer before the bell is set

at the surface. In this way a slag free surface of the steel melt is created inside the bell. Alloying materials can be fed in an inert argon atmosphere into the clean steel surface without slag. The slag may attach to the bell but this can be minimized by controlling the slag viscosity and melting temperature (H.-M. Wang et al., 2007).

A steel melt batch can be heated by feeding aluminium and oxygen inside the bell. Oxygen is delivered to the melt surface with a lance, typically equipped with a convergent divergent de Laval nozzle to achieve a supersonic flow. Aluminium particles are simply dropped onto the melt surface inside the bell. A typical heating rate is about 10 K/min, ranging between 5-13 (Audebert et al., 1989) and 9-15 (Nilsson, Andersson, & Lindquist, 1996) depending on the installation. It is possible to heat up to 90 K at one instance (Stolte, 2007, 118), but it is recommended to keep the maximum to 30 K to prolong the bell life (Nilsson et al., 1996). Nilsson et al. (1996) describe their experiences of CAS-OB at SSAB Tunnsplåt in Sweden. They heated 25% of the heats and claim that the CAS-OB install has been a success by increasing production, lowering costs and improving quality.

### **1.3 Aims of this study**

The objective of this thesis is to study supersonic lances and to create a process model of the CAS-OB heating stage. For successful execution CFD (computational fluid dynamics) simulations are needed, as well as experimental work for model validation. Results of supersonic lance studies are useful in many metallurgical processes that include a top lance. A CAS-OB heating stage process model is needed in process development and as a research tool.

The aims of this work are:

1. To develop and validate supersonic lance CFD model.
2. To calculate heat and mass transfer coefficients for supersonic lances.
3. To develop and validate a CAS-OB heating stage model.

Papers I and III study the lance blowing by CFD while the CAS-OB heating stage modelling is covered in papers II and IV. The role of individual papers is presented in Figure 2.

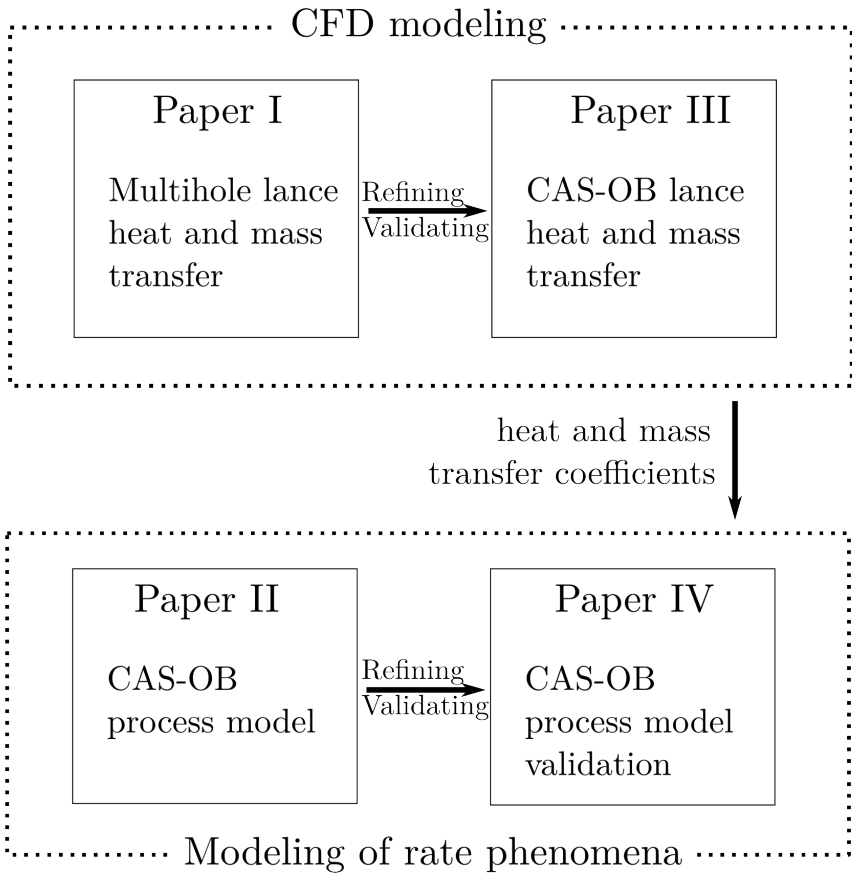


**Fig. 2. Role of the individual publications in the study.**

## 1.4 Work outline

The contents of this thesis are defined by the aims of the work and their realization. The first aim is “To development and validate a supersonic lance CFD model”. A CFD model is needed because of the following demands for the lance model:

1. Prediction of the flow in different geometries of nozzles and under different operating conditions.
2. Determination of the heat and mass transfer rate to the melt surface.

The lance jet is turbulent, and the properties of the flow are to large extent defined by the turbulence. Therefore it is necessary to find a suitable turbulence model by testing with experimental data. The developed CFD models are used to fulfil the second aim: “To calculate heat and mass transfer coefficients for supersonic lances”. While some heat and mass transfer correlations can be found in the literature, CFD simulations can be used to calculate heat and mass transfer coefficients specifically for a needed case. This is utilized in the present work.

For a successful realization of the process model in the third aim, “To develop and validate a CAS-OB heating stage model”, the following demands must be satisfied:

1. Reaction modelling
2. Mass conservation
3. Energy conservation
4. Reasonable calculation time

The calculation speed limits the number of computational nodes or cells; a CFD model is not an option. Instead a specific software program was developed using c++ that includes mass and energy conservation systems, descriptions for heat and mass transfer rates and a model for the reaction system.

This thesis first presents some literature research on supersonic lance and CAS-OB modelling in order to provide some background to the work and to view it from a larger perspective. Then the CFD models, the heating stage process model and industrial experiments are explained. Finally, the results are presented and compared to experimental data for model validation.



## 2 Literature section

### 2.1 Supersonic lances

Supersonic lances are used for greater jet penetration compared to subsonic lances. Better reach of the gas jet is induced by higher velocity and a potential core, in which the velocity is nearly constant. After that there is still some supersonic flow in a part called supersonic core (Chatterjee, 1972). When the jet velocity goes below the speed of sound, the jet decays like a subsonic jet. The flow from a single de Laval nozzle is presented in Figure 3. the velocity of the gas is subsonic before the throat flow area, where it reaches the speed of sound and is supersonic in the diverging area.

Thermodynamics set the limits for de Laval nozzle in supersonic lance heads, the key factor is the gas compressibility. For an ideal gas

$$P = \rho R_g T, \quad (1)$$

where  $R_g$  is the specific gas constant, which has following relation to a universal gas constant  $R$

$$R_g = \frac{R}{M}. \quad (2)$$

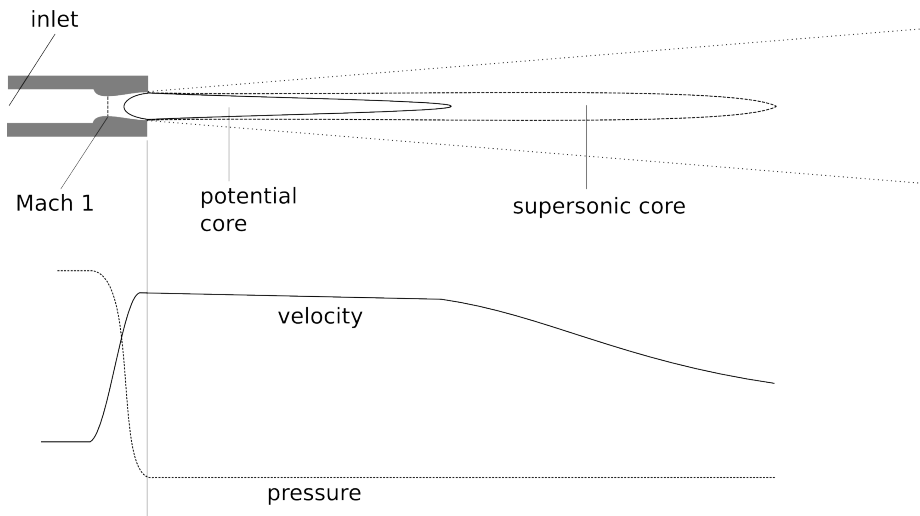


Fig. 3. Supersonic jet.

M is mole mass of the gas. The gas constant can also be expressed with a specific heat at constant pressure  $c_p$  and specific heat at a constant volume  $c_v$  as

$$R_g = c_p - c_v. \quad (3)$$

The ratio of specific heats is  $\gamma$ ,

$$\gamma = \frac{c_p}{c_v}. \quad (4)$$

A Bernoulli equation in one dimension for frictionless flow is

$$u \, du + \frac{1}{\rho} = 0. \quad (5)$$

From these principles and the fact that the mass flow rate is the same in the whole length of the nozzle, equations 6, 7 and 8 can be formulated.

The maximum mass flow rate through de Laval nozzle can be formulated from the Bernoulli equation as (Douglas, Gasiorek, & Swaffield, 1986, 522)

$$\dot{m} = \frac{A_t p_0}{\sqrt{T}} \sqrt{\frac{\gamma}{R_g} \left( \frac{2}{\gamma+1} \right)^{(\gamma+1)/(\gamma-1)}}, \quad (6)$$

where  $A_t$  is nozzle throat area and  $p_0$  is inlet pressure.

If the nozzle is designed so that the exit pressure  $p_e$  equals the ambient pressure, the exit velocity is (Geiger & Poirier, 1973, 161)

$$Ma_e^2 = \frac{2}{\gamma-1} \left( \frac{p_0^{(\gamma-1)/\gamma}}{p_e} - 1 \right), \quad (7)$$

where  $Ma$  is Mach number,  $Ma = u/c$ , and  $c$  is speed of sound  $c = \sqrt{\gamma R_g T}$ .

When the nozzle is working properly  $Ma = 1$  at the throat area, and following relation for the areas of the throat  $A_t$  and exit  $A_e$  applies (Deo & Boom, 1993, 26):

$$\frac{A_t}{A_e} = \left( \frac{\gamma+1}{2} \right)^{1/(\gamma-1)} \left( \left( \frac{\gamma+1}{\gamma-1} \right) \left( \left( \frac{p_e}{p_0} \right)^{2/\gamma} - \left( \frac{p_e}{p_0} \right)^{(\gamma+1)/\gamma} \right) \right)^{1/2}. \quad (8)$$

When designing a lance head, the inlet pressure can be first solved from Equation 7 for desired output velocity. Then the throat area can be calculated from Equation 6 with the desired maximum flow rate. The exit area is then given by Equation 8.

Isentropic theory can be used in lance nozzle design to determine the throat and exit areas, but the lengths and the shape of the sections have to be decided by other means. The angle of divergence must be quite low to keep the flow from separating from the

nozzle wall. A value of around  $7^\circ$  is often used for this purpose (Geiger & Poirier, 1973, 161).

The shape can be determined with the method of characteristics (MOC). The basis for optimization is to usually calculate a minimum length for the nozzle, to avoid excess friction. Bhattacharya, Zhan, and Chukwulebe (2015) used MOC in BOF lance design and tested the design with CFD simulations. They also found that the shape of the convergent part of the nozzle is not very important, but the diverging part dictates the nozzle performance.

A supersonic lance works properly only with the correct oxygen feed. If the pressure is not what the nozzle is designed for, shock waves will occur. If the feed pressure is too low, the gas expands too much in the divergent section of the nozzle and pressure at the exit becomes lower than the ambient pressure. This is called over expansion. If the pressure is too high, under expansion happens and the gas pressure becomes too high at the exit. In both cases shock waves are formed because of the pressure discontinuity, which can cause excessive wear to the lance head. An over expanded jet can especially cause erosion if the hot gas from the environment reaches the nozzle interior. In a steel mill, a precisely correct inlet pressure is not practically possible to maintain, and therefore it is safer to keep the pressure on the high side and the jet slightly under expanded. Higher inlet pressure will also produce a higher velocity jet, which can be desirable in steel production (Koria, 1988). Otherwise the jet is similar to a correctly expanded jet. Koria and Lange (1984) found that the subsonic part of an under expanded jet's axial velocity decays in exactly the same way as in the fully expanded flow.

In metallurgical processes the lance head can have a single nozzle or several nozzles. Multi-hole lances are dominant in converter processes and popular numbers of nozzles are 3-6. According to Smith (1966), the benefits of multi-hole lances are their smoother performance, less material ejected out from the furnace and better material yield, when compared to a single hole lance at the same flow rate. Single and multi-hole lances have different optimum distances from the melt surface but they both have the same impact area from their optimum height. The optimum height for single-hole lances is higher than the multi-hole lances optimum height, and therefore the jet penetration is greater with multi-hole lances. In general, single hole lances are used in applications with low gas flow rates and multi-hole lances with higher gas flow rates.

The jets of a multi-hole lance tend to bend inwards and coalesce if the inclination angle is low. The angle is in-between the nozzle centreline and the lance head centreline.

Usually the nozzles are placed symmetrically. The minimum angle that prevents the jets from merging is  $10^\circ$  (Smith, 1966) or  $11^\circ$  (Lee, O'Rourke, & Molloy, 2002).

In 2006 Odenthal, Falkenreck, and Schlüter (2006) modelled compressible supersonic lance flows separately and then corrected the results to corresponding flow with incompressible gas phase. A normalized momentum force  $\rho u^2$  was used as a similarity criterion. The whole converter was then simulated with incompressible phases. This is because a compressible flow with a multiphase model is a sensitive system, and in practice calculation is impossible. They used a DPM (discrete phase model) to describe the gas bubbles from bottom blowing and a VOF multiphase method for melt surface flow. In this way, the cell size in the computational mesh can be larger than the bubble size, making the calculation possible with practically sized meshes. Only the splashing phenomenon cannot be solved accurately because mesh resolution is not sufficient. The lance flow was validated only inside the nozzle, by comparing the CFD results to calculation results by isentropic theory. A good match was found. They note that CFD modelling is still challenging in metallurgy, especially in the case of simultaneous compressible gas flows and multiphase flows with high densities.

A similar kind of simulation was done later by Y. Li, Lou, and Zhu (2012) who also combined DPM and VOF. Their simulated results of supersonic lance match the experimental data quite precisely.

Alam, Naser, and Brooks (2010) used CFD in a study on supersonic jets at steelmaking temperatures. They used a modification to the k- $\epsilon$  turbulence model in order to better match the high temperature measurement data of Sumi, Kishimoto, Kikuchi, and Igarashi (2006). They found that in steelmaking temperature 1800 K, the potential core length of the jet was 2.5 times the core length of the same jet at room temperature. They also noted that the droplet generation rate was higher at high temperatures. They did not calculate the flows in the nozzle itself as the inlet of the computational domain is the exit of the nozzle. This is understandable, because Sumi et al. (2006) did not publish the nozzle geometry. The turbulence created by the details of the nozzle geometry was not taken into account. Allemand, Bruchet, Champinot, Melen, and Porzucek (2001) claim that the nozzle design has a major effect on the created turbulence and therefore also on the jet behaviour.

Sumi et al. (2006) note that it is difficult to obtain a homogenous ambient temperature in an experimental setup, and they used the temperature outside the jet in the radial direction as the ambient temperature. This is not a trivial matter, since the supersonic jet

**Table 1. Top lance CFD models.**

Author	Multiphase	Turbulence	Validation	Bubbling	Process
Odenthal et al. (2006)	VOF, DPM	k- $\epsilon$	theory	yes	BOF
Ersson, Tilliander, et al. (2008)	VOF	k- $\epsilon$ mod	water model	no	BOF
Alam et al. (2010)	-	k- $\epsilon$ mod	experiment	-	-
W. Wang et al. (2010)	-	k- $\omega$ , k- $\epsilon$	experiment	-	BOF
Y. Li et al. (2012)	VOF, DPM	k- $\epsilon$	experiment	yes	BOF
Q. Li et al. (2014)	VOF	k- $\epsilon$	experiment	no	BOF
Q. Li et al. (2015)	VOF	k- $\epsilon$	water model	no	BOF
Kärnä et al. (Paper III)	-	k- $\epsilon$ mod	experiment	no	CAS-OB
M. Li et al. (2016)	VOF	k- $\epsilon$	no	no	BOF

itself is very cold compared to the hot ambient temperature and it has a cooling effect on the ambient temperature.

Q. Li, Li, Kuang, and Zou (2014) studied the interaction of supersonic jets and the melt in a BOF. They found that their CFD results for supersonic lance simulations were within a 2% margin of error compared to calculations by isentropic theory. They used a standard k- $\epsilon$  turbulence model. Furthermore, in their work it was found that the hot ambient temperature causes a higher jet velocity and lower density, but the jet dynamic pressure is not changed significantly. They observed splashing with the volume of fluid multiphase model, but the density of the computational mesh was not adequate for droplet size determination. In another paper on the same subject they compared the CFD results to water model results and found a reasonably good agreement (Q. Li, Li, Kuang, & Zou, 2015). Momentum and kinetic energy were found to have a low transfer rate between the jets and the molten bath. About half of the total momentum transferred into the bath goes into the slag layer and half into the steel melt. The melt viscosity and surface tension have only a minor effect on the behaviour of the slag and melt compared to the lance height and operating pressure. In another paper (M. Li, Li, Kuang, & Zou, 2016), the same authors also found that their CFD simulation predicts about a 20% higher penetration into the melt than the correlation by Koria and Lange (1987), which is actually a quite good match.

W. Wang et al. (2010) compared k- $\omega$  and k- $\epsilon$  turbulence models in a CFD model of a four-hole lance. They claimed that k- $\omega$  model was better, but the comparison is difficult since the experimental data and each modelling result is in a separate plot and the experimental data is for a three-hole lance. The conclusion is that the turbulence models produced different results and the jets bent towards each other.

Ersson, Tilliander, et al. (2008) modified the standard k- $\epsilon$  turbulence model by adjusting one of the parameters,  $C_{\epsilon 2}$ , for better jet penetration. The studied case was a scale model of a top-blown converter with a subsonic lance. The modification made a difference and the modified model was compared to the standard and realizable k- $\epsilon$  turbulence model. All turbulence models give reasonable results related to the water model data and literature data, but none of them were perfect. They showed that turbulence models can be tweaked, but did not proceed further in matching the model to the data.

In conclusion, a number of models exists, and some of the relevant ones for this work are reviewed here and summarized in Table 1. Most of the existing CFD models use a standard k- $\epsilon$  turbulence model, and if liquid phases are involved a VOF multiphase model is used. Ansys Fluent is the most popular software used.

Experimental models or data on supersonic lance are very limited. There are a number of experimental models applied to supersonic lances, but the actual experiments have been made with subsonic jets. Chatterjee et al. (Chatterjee, Wakelin, & Bradshaw, 1972; Chatterjee & Bradshaw, 1973) studied mass transfer with a liquid silver model and resulted in correlations for mass transfer, which are interesting but with a limited usability for supersonic lance processes. Lohe (1966, 1967) carried out experiments where the mass transfer was measured by the water evaporation rate, caused by the air jet. Based on the measurements, Oeters (1994, 172) published the following correlation

$$Sh = 1.41Re^{0.51}Sc^{0.33}, 2 \times 10^3 \leq Re \leq 3 \times 10^4, \quad (9)$$

$$Sh = 0.41Re^{0.75}Sc^{0.53}, 3 \times 10^4 \leq Re \leq 2 \times 10^5. \quad (10)$$

Where the length and velocity for the Reynold number are impact area diameter and velocity, which have to be known or calculated by other correlations.

Also the jet penetration models by Wakelin (1966)

$$H_0 = \frac{7.6d_0^2\rho_g U_0^2}{2g\rho_l H^2} / \left( \frac{H + H_0}{H} \right)^2, \quad (11)$$

where  $H$  is lance height and  $H_0$  is the depth of the cavity, and Koria and Lange (1987)

$$H_0 = 4.469 \left( \frac{0.7854d^2 p_a (1.27 p_0 / p_a - 1) \cos \alpha}{\rho_l g H^3} \right)^{0.66} \quad (12)$$

are based on experimental data on subsonic jets, but they are applied also for supersonic jets. The model by Koria and Lange was tested with a variety of experimental data

and it provides good agreement, and by assuming that the subsonic and supersonic jet penetration properties follow the same mechanisms, it can be used for supersonic lances.

A valuable experimental data-set for supersonic lance was actually made for a NASA (National Aeronautics and Space Administration) rocket nozzle test (Eggers, 1966), the design of the nozzle is close to the one used in lances for steelmaking, and the size approximately the size of the lance used in the CAS-OB process. Another data source for a supersonic experiment was made by Sumi et al. (2006), who measured the jet in hot ambient temperatures. However, they did not publish the nozzle geometry, which is available for the rocket nozzle (Shoemaker, 1965).

## 2.2 Reaction modelling

In this section some different ways of modelling reactions in metallurgical processes are presented together with example studies of each type. The examples are chosen from processes that have some similarities to the CAS-OB process.

Chemical reactions can be modelled in many ways, here they are categorized as:

1. Models with explicit reaction rate descriptions
2. Chemical equilibrium models
3. Indirect models

The first category is useful when the reaction mechanism is known and relatively simple, with not many simultaneous reactions. An example of a suitable phenomenon to be modelled using simple rate equations would be nitrogen dissolution into a steel melt. This can be modelled with a couple of rate equations. The phenomenon is slow and not very dependent on other reactions. This type of models has been used also for modelling more complex systems, where their performance is not always easy to judge.

Chemical equilibrium models are often equipped with Gibbs energy minimization for equilibrium state calculation. Lagrangian multipliers can be used to solve the constrained minimization problem (Eriksson, 1971). The system does not need information about the reaction mechanisms, only the possible species that might appear from the reactive system. Pure equilibrium calculation do not take time into account, therefore they are best suited for systems with fast reactions and good mixing.

Often a limiter is introduced into chemical equilibrium models, to better take into account time-dependent phenomena. Only a small volume can be put into a chemical equilibrium to simulate a reaction zone, and the mass transfer to this volume acts as a

limiting step. The limiting factor may be something else too, as is noted in the work of Koukkari and Pajarre (2011).

The third category includes everything else not in the first two categories, such as the law-of-mass-action-based method by Järvinen et al. (2016) and oxygen distribution by affinity in models by Wei and Zhu (2002) and Jalkanen (2006).

In the following part some reaction models relevant to lance processes are presented, the model by Ersson, Höglund, Tilliander, Jonsson, and Jönsson (2008) is an example of a chemical equilibrium model while Dogan, Brooks, and Rhamdhani (2011b) are representing an explicit reaction rate approach and Järvinen et al. (2016) an indirect model.

### **2.2.1 Chemical equilibrium model**

Ersson, Höglund, et al. (2008) combined CFD simulations with thermodynamic software, using the Fluent and Thermo-Calc software packages. Their idea was to put each computational cell into equilibrium if it contains multiple phases. The composition and temperature of the cell was sent to Thermo-Calc, which calculated the equilibrium composition, and the data was then sent back to Fluent, where the new composition was explicitly set into the cell. Mass changes were handled by adding source terms to Fluent's conservation equations for the next time step. This happened at every time step or at every  $n$ th time step to save computational effort.

It was assumed that the reaction rates were limited by mass transfer and the mass transfer rate inside the reacting computational cell was infinitely fast. Therefore, the mass transfer between the cells determines the reaction rate, which means that large scale mass transfer dominates because the computational cells are macroscopic in size. With a denser mesh smaller scales are reached, but in practice the computation soon becomes impossible because of the computational load.

The computational domain was a 2-dimensional scale model of a BOF converter, sized  $0.075 \text{ m} \times 0.13 \text{ m}$ , the same as in a physical model. A VOF multiphase model with  $k$ - $\epsilon$  turbulence model were used in the flow calculation. The simulation was for steel at  $1500 \text{ }^\circ\text{C}$  with subsonic oxygen blowing. The gas was modelled as incompressible but the gas density used does not correspond to the temperature of the metal bath. They calculated the blowing for 5 seconds and then extrapolated the results to 15 minutes and compared it to experimental results.

The conclusions regarding the real process are slightly far-fetched, but the main result of the study was to show that this kind of combination of software is possible, and in the future could be used for real work. The concept is appealing since it can be implemented by using existing software and there is no need to know the geometry or area of the reaction surfaces. The drawbacks are dependency on computational grid size and the explicit composition update, which require a dense grid and small time-step, respectively. This demands vast computing power. Some practical limits could be found for accuracy and computational load but they were not studied. A similar system has been applied for an AOD converter by Andersson, Tilliander, Jonsson, and Jönsson (2013), but without a top lance.

### 2.2.2 Model with explicit reaction rate descriptions

Dogan et al. (2011b), modelled decarburization in the oxygen jet impact zone, which is a part of their oxygen steelmaking model (Dogan, Brooks, & Rhamdhani, 2011a). The reactions were modelled with explicit rate equations. In a situation with a high carbon content in the steel melt, the decarburization occurs through two reactions, via CO<sub>2</sub> and O<sub>2</sub>. The CO<sub>2</sub> reaction rate was determined by mass transfer rate and chemical rate:

$$-\frac{dW_c}{dt} = 100M_c A k_a p_{CO_2}, \quad (13)$$

where the rate constant

$$k_a = \frac{1}{RT_f/h_{m,g} + 1/k_c}. \quad (14)$$

$M_c$  is molar mass of carbon,  $k_a$  is the apparent rate constant,  $h_{m,g}$  gas phase mass transfer coefficient and  $k_c$  the chemical rate constant of the reaction. The reaction by oxygen is limited by mass transfer in gas phase,

$$-\frac{dW_c}{dt} = 200M_c A h_{m,g} \ln(1 + p_{O_2}). \quad (15)$$

In a case when carbon content is below critical level, carbon mass transfer in the melt is assumed to control the decarburization rate.

$$\frac{dW_c}{dt} = h_m A \frac{\rho_m}{100} (\text{mass}\%C_b - \text{mass}\%C_{eq}). \quad (16)$$

The equilibrium carbon content  $C_{eq}$  was not calculated but assumed to be so small that it could be neglected. The gas mass transfer coefficient was calculated with a correlation

proposed by Oeters (1994, 172) from data by Lohe (1966), presented in Equations 9 and 10.

In the reaction model, energy conservation was not solved, the gas and reaction zone temperature values were set by assumptions and the film temperature was calculated as a mean value of the two. The reaction area was assumed equal to the area of jet penetration. The shape of the depressions was assumed to be paraboloid. Based on the modelling results the authors claimed that 40% of the decarburization takes place at the impact zone.

### 2.2.3 Indirect model

The method by Järvinen et al. (2016) is based on the idea that all reactions are limited by mass transfer and a limited chemical equilibrium is present at the reaction surface. For an elementary reaction



where  $v_i$  is the stoichiometric coefficient of substance  $i$ , the forward reaction rate is

$$R_f = k_f a_A^{v_A} a_B^{v_B} \quad (18)$$

and the backward rate is

$$R_b = k_b a_D^{v_D} a_E^{v_E}, \quad (19)$$

where  $a_i$  is the activity of species  $i$ , and  $k_f$  is forward reaction rate coefficient and  $k_b$  backward reaction rate coefficient.

In equilibrium

$$k_f a_A^{v_A} a_B^{v_B} = k_b a_D^{v_D} a_E^{v_E}, \quad (20)$$

and thus

$$\frac{k_f}{k_b} = \frac{a_D^{v_D} a_E^{v_E}}{a_A^{v_A} a_B^{v_B}}. \quad (21)$$

The equilibrium constant is

$$K = \frac{k_f}{k_b} = \frac{a_D^{v_D} a_E^{v_E}}{a_A^{v_A} a_B^{v_B}}. \quad (22)$$

If the reaction is not in equilibrium, the net reaction rate is

$$R = R_f - R_b = k_f a_A^{v_A} a_B^{v_B} - k_b a_D^{v_D} a_E^{v_E}. \quad (23)$$

With K this can be expressed as

$$R = k_f \left( a_A^{v_A} a_B^{v_B} - \frac{1}{K} a_D^{v_D} a_E^{v_E} \right). \quad (24)$$

When the reaction rate is limited by mass transfer, the mass transfer rate equals the reaction rate. For a single component, for example A, this means

$$h_A \rho (y_{A,bulk} - y_{A,surface}) = k_f \left( a_A^{v_A} a_B^{v_B} - \frac{1}{K} a_D^{v_D} a_E^{v_E} \right) v_A^*, \quad (25)$$

where  $y_A$  is mass fraction of component  $i$ ,  $h_A$  is the mass transfer coefficient of component A and  $v_A^*$  is mass-based stoichiometric coefficient. If we assume that the reaction rate is limited by mass transfer rate, and not by the forward reaction rate coefficient  $k_f$ , the  $k_f$  can be infinitely big. This means that the chemical equilibrium term approaches zero when  $k_f$  approaches infinity. This is the core of the method. In the iterative calculation, the reaction rate changes the amounts of species  $y_i$  and thereby the activities  $a_i$  so that the term inside the parentheses comes closer to zero (equilibrium) when  $k_f$  approaches infinity. In numerical solution the  $k_f$  cannot be infinite but a very large number is needed.

For modelling the example reaction, four conservation equations similar to 25 are needed, one for each component. In addition to these, the bulk mass fractions are also unknown, which yields four more conservation equations. When adding more reactions to the system, more equations are needed. Additionally, because different reactions can depend on the same components, all equations must be solved simultaneously. In the case of multiple reactions, the mass conservation term of component A at the reaction surface becomes

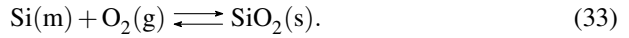
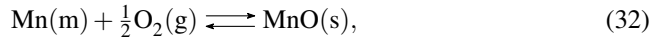
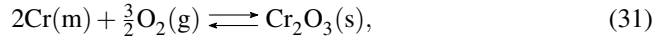
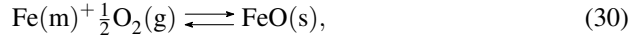
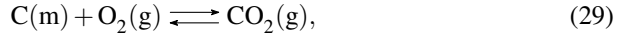
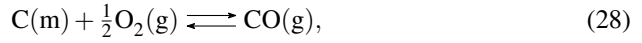
$$h_A \rho (y_{A,bulk} - y_{A,surface}) = \sum_{i=1}^n R_i v_A^*, \quad (26)$$

where  $R_i$  is the reaction rate of reaction  $i$ .

The challenging part of the method is handling the values of  $k_f$ , that need to be large enough to get the reaction surface composition to almost chemical equilibrium. Sometimes very large values are needed, causing computational instabilities.

A detailed reaction model for top lance blowing in an AOD converter was proposed by Visuri et al. (2017a). The model is based on the reaction modelling method by Järvinen et al. (2016). The top blowing model was developed and validated (Visuri et al., 2017b) as a stand-alone model but it was intended to be combined with an earlier-proposed model for reactions during side-blowing (Järvinen et al., 2011; Pisilä et al., 2011).

The following reactions are included in the model:



Additionally N, Ni, Al, S, N<sub>2</sub>, Ar, CaO, MgO, Al<sub>2</sub>O<sub>3</sub>, CaO and generic residual oxide MeO<sub>x</sub> are included in the model as inert species.

In the model, reactions take place at two massless reaction interfaces, at the melt surface of the jet-induced cavity of and at the steel droplet surface. The steel droplets are generated from lance blowing and react while sinking back into melt bath through the slag layer. The droplet generation rate, droplet size distribution and droplet residence time are solved as well as the cavity surface area. The cavities created by the gas jets are assumed to be non-coalescing and their geometries are given according to the correlation by Koria and Lange (1987).

In the model, mass conservation is based on the balance in between the mass transfer to the reaction fronts and the net reaction rate. Also, the Stefan flow is taken into account, which is the effect of the bulk flow caused by all reactions.

Mass transfer coefficients are modelled with an appropriate correlation for each situation. The lance blowing mass transfer is modelled with a correlation from Oeters (1994) based on data by Lohe (1966) in a similar way to Dogan et al. (2011b). The thermodynamic modelling is also detailed, and the the Gibbs energy is calculated with a Shomate equation and several activity models are used. The UIP (Unified Interaction Parameter) model is used for metal species and a model proposed by Wei and Zhu (2002) for slag species.

In the computation forward rate coefficients  $k_f$  are increased at each time step until the equilibrium number criterion is satisfied (Visuri et al., 2017a),

$$E = \left| 1 - \frac{Q}{K} \right| < 0.001. \quad (34)$$

where  $Q$  is reaction quotient and  $K$  is equilibrium constant. This takes some time, and typically one time step takes a few seconds to finish.

#### **2.2.4 Models of the CAS-OB process**

Ha and Park (2008) studied ladle flow phenomena in CAS-OB by creating a physical model prior to the CAS-OB start up at POSCO. They tried two bell sizes, and the bell diameter was found to have only a minor effect on mixing time. The bell immersion depth on the other hand had a major impact on the mixing, and a deeper immersion caused a longer mixing time. They also found that the mixing was best when the bell was not used. The mixing time was found to decrease as bottom blowing was increased. Inclusion removal was studied by placing small floating plastic particles inside the bell and calculating their number during experiments. Higher bottom blowing enhanced the inclusion removal, while higher top blowing rate hindered the inclusion removal. Their conclusion was that in CAS-OB operation it is essential not to position the bell lower than needed and to have high bottom blowing rate.

Ma, Bao, Zhao, and Wang (2014) studied CAS-OB mixing time by physical model of ratio 1/4.5 of a 300-ton ladle and bell, by varying the bottom bubbling flow rate and the location of bottom bubbling, with oil describing the slag layer. They found that mixing was best in one location of the bottom bubbling nozzle, at 0.3 ladle radius from the ladle centre. As a function of the gas flow rate the mixing time first decreased as expected but after a certain point the mixing time started to steeply increase again. The authors suspect it might be caused by the bell. They also conducted some trials at a steel plant according to their findings with a new bottom plug position and slightly higher gas flow rate, and a performance improvement was reported.

Some more research has been made on the CAS-process (Composition Adjustment by Sealed Argon Bubbling), which is partially applicable to CAS-OB. Pan et al. (1994) conducted a water model study on the mixing time and fluid flow pattern in CAS. They found that the flowrate enhanced mixing, but bottom bubbling position was not as crucial in their case compared to the findings by Ma et al. (2014). They found that there was a certain critical flow rate, where a higher flowrate caused the bubble plume to exceed the baffle (a part in the surface similar to the bell in CAS-OB) area and possibly cause melt exposure to the atmosphere outside the baffle. They concluded that the fluid flow was significantly different in CAS compared to the ladle in bottom stirring, and the deeper the baffle is in the melt the longer the mixing time. Eccentric placing of the bottom plug and the baffle are recommended, together with a high bubbling rate and the usage of ladles with higher height/diameter ratios than 1.2.

Mazumdar and Guthrie (1995) studied melt flows in the CAS process in 1995 using CFD. From the resulting flow fields, it can be seen how the baffle stops the flow circulation. The maximum number of computational cells was 648 in their study, today it is common to use about 1000 times more cells in a simulation of a similar system.

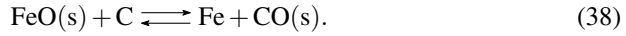
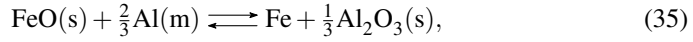
The ladle used in the CAS-OB process is a conventional ladle. There are a lot of modelling studies for ladle flows and heat transfer that apply to some extent to the CAS-OB process. However, as determined in the scale model studies, the steel melt flow pattern is retarded by the flow when the bell is in use. Heat transfer through the ladle walls is practically the same regardless of the mixing rate because the steel heat transfer rate is much higher than the ladle refractory heat transfer rate.

T. Fredman and Saxen (1998) made a model for temperature profile in ladle walls and applied thermocouple measurement validation. They also made a simulating tool for ladle temperature prediction (T. P. Fredman, Torrkulla, & Saxen, 1999).

Recently Kulju, Ollila, Keiski, and Muurinen (2013, 2015) studied fluid flows in the CAS-OB ladle with CFD simulations. With dense meshes (up to 2.2 million cells) the slag open eye formation could be studied in detail. However, the bell was not included, but a situation when the bell is uplifted was simulated. Interestingly the simulations were made with open source software OpenFOAM, using a hybrid multiphase model that uses Eulerian formulation for the bubbly flow and a VOF (volume of fluid) method for free surface and slag layer tracking. This way the computational mesh does not need to resolve the bubbles in the melt. They are handled by the Eulerian model. The simulations were validated with experimental data from the literature and good agreement was found. It would be useful to use their model to simulate CAS-OB with a bell to study fluid flows during the heating stage.

A mathematical model for the reduction stage of the CAS-OB process has been developed by Sulasalmi et al. (2016). Their model focuses on the reduction stage at the end of the process, after an optional heating stage. A reaction model was based on the method by Järvinen et al. (2016), where the reaction rates are limited by mass transfer. The reaction system consists of following reactions, occurring at the steel-slag droplet

interface:



Ni, CaO and Ar are assumed not to participate in the reactions, but they are taken into account in the mass transfer and activity calculations. It is assumed that the selection of reactions is irrelevant, as long as all the needed components are included and have the ability to affect to the entire system. This is achieved by solving the system simultaneously.

The equilibrium condition is monitored with an equilibrium number (Equation 34) in the same way as in the study of Visuri et al. (2017a). In this case, the forward rate coefficients  $k_f$  can be set to be large enough before the calculation, which is not possible in all systems, when the coefficient needs to be increased during iterations.

In the model, mass is conserved in all phases in the same manner and the mass transfer in between the bulk and the reaction surface equals the net reaction rate. The conservation of heat takes into account heat losses through the ladle and the bath surface as well as the heat of the reactions.

An important part of the model is slag emulsification, which has been studied by means of CFD simulations (Sulasalmi, Kärnä, Fabritius, & Savolainen, 2009; Sulasalmi, Visuri, & Fabritius, 2013; Sulasalmi, Visuri, Kärnä, & Fabritius, 2015) for this purpose. The rate of slag droplet formation was determined as well as their size distribution.

The results from the reduction stage model were compared to industrial data and were in good agreement both concerning the chemical composition and temperature. It was found that the exothermic reactions have a minor effect on the cooling of the steel melt compared to the cooling from the melt surface. The reaction system for slag reduction in CAS-OB seems to be well suited for the reaction calculation method by Järvinen et al. (2016) because it is not necessary to change the  $k_f$  values during calculation. The calculation of the whole reduction stage takes some seconds, which is in the same order of the time needed to calculate one time step of AOD lance model by Visuri et al. (2017a, 2017b).



## 3 Methods

In this chapter the research work done for this thesis is presented.

### 3.1 CFD modelling

Computational fluid dynamics (CFD) can be thought of as the use of computers to produce information about fluid flows in given situations (Shaw, 1992, v). It can also be considered as a sub-field of either fluid dynamics or numerical analysis (Ferziger & Peric, 1996, 20). CFD simulations have been used since the 1960s to predict fluid flow phenomena. First it was used mainly for the aerospace industry, but later for a wide variety of applications that include fluid flows (Versteeg & Malalasekera, 2007, 1). CFD simulation includes three parts:

1. Meshing involves creating the computational geometry and dividing the geometry into computational cells, resulting in a mesh.
2. Solving means computing the results in the computational mesh, using appropriate models and algorithms, boundary conditions and material properties.
3. Post-processing is used to visualize the results of the computation.

Each part can be done with separate software or in some cases all steps are possible within the same software.

There are three main solution methods for the CFD solver software (Ferziger & Peric, 1996, 25):

1. Finite difference
2. Finite volume
3. Finite element

The difference between the methods is especially in the discretization, which means approximating differential equations by replacing them with algebraic equations at discrete locations. The finite volume method is used in this work and the algorithm has the following three steps:

1. Creating a set of equations by integrating fluid flow equations in each control volume in the system.

2. Discretising the equations by replacing the integrals with approximations, creating a system of algebraic equations.
3. Solving the system of algebraic equations.

In the finite volume method, the computational domain is divided into control volumes, and the variable values are at the centre of the volumes. The values of variables at the control volume walls are interpolated from centre values. In this work the finite volume method is applied with Ansys Fluent software package.

### 3.1.1 Conservation equations

The conservation system used in Ansys Fluent software package is briefly presented (Ansys Inc., 2009). The conservation of mass

$$\frac{\partial \rho}{\partial t} + \nabla \cdot (\rho \vec{v}) = S_m, \quad (39)$$

$S_m$  is the mass source term. The conservation of momentum is

$$\frac{\partial}{\partial t} (\rho \vec{v}) + \nabla \cdot (\rho \vec{v} \vec{v}) = -\nabla p + \nabla \cdot (\bar{\tau}) + \rho \vec{g} + \vec{F}, \quad (40)$$

where  $\vec{F}$  is a source term for additional force and  $\bar{\tau}$  is the stress tensor,

$$\bar{\tau} = \mu \left[ (\nabla \vec{v} + \nabla \vec{v}^T) - \frac{2}{3} \nabla \cdot \vec{v} I \right]. \quad (41)$$

$\mu$  is viscosity and  $I$  is the unit tensor.

The conservation equation for any scalar  $\phi$  is

$$\frac{\partial \rho \phi}{\partial t} + \frac{\partial}{\partial x_i} (\rho u_i \phi - D_\phi \frac{\partial \phi}{\partial x_i}) = S_\phi, \quad (42)$$

where  $D_\phi$  is diffusion coefficient and  $S_\phi$  source term.

The conservation of energy is handled by the equation

$$\frac{\partial}{\partial t} (\rho E) + \nabla \cdot (\vec{v} (\rho E + p)) = \nabla \cdot \left( \lambda_{eff} \nabla T - \sum_j h_j \vec{J}_j + (\bar{\tau}_{eff} \cdot \vec{v}) \right) + S_E, \quad (43)$$

where  $\lambda_{eff}$  is the effective conductivity, a sum of the conductivity and turbulent conductivity  $\lambda + \lambda_t$  and  $S_E$  is the energy source term.

The momentum of continuous phase  $q$  of the Eulerian multiphase model is conserved as

$$\begin{aligned} \frac{\partial}{\partial t}(\alpha_q \rho_q \vec{v}_q) + \nabla \cdot (\alpha_q \rho_q \vec{v}_q \vec{v}_q) = & -\alpha_q \nabla p + \nabla \cdot \bar{\tau}_q + \alpha_q \rho_q \vec{g} \\ & + \sum_{p=1}^n (K_{pq}(\vec{v}_p - \vec{v}_q) + \dot{m}_{pq} \vec{v}_{pq} - \dot{m}_{qp} \vec{v}_{qp}) + \vec{F}_q + \vec{F}_{lift,q} + \vec{F}_{vm,q}, \end{aligned} \quad (44)$$

where  $\vec{F}_q$  is external body force  $\vec{F}_{lift,q}$  is lift force and  $\vec{F}_{vm,q}$  is virtual mass force.  $K_{pq}$  is momentum transfer coefficient between phases,

$$K_{pq} = \frac{3}{4} \frac{\alpha_q \alpha_p \rho_q |\vec{v}_p - \vec{v}_q|}{d_p} C_D, \quad (45)$$

where  $\alpha_q$  is the volume fraction of the continuous phase,  $\alpha_p$  is the volume fraction of the dispersed phase, and  $\rho_q$  is the density of continuous phase. The drag coefficient  $C_D$  can be described with a suitable model, for example in the Schiller-Naumann model

$$C_D = \begin{cases} 24(1 + 0.15 Re^{0.687})/Re & Re \leq 1000 \\ 0.44 & Re > 1000 \end{cases}, \quad (46)$$

where the Reynolds number is

$$Re = \frac{\rho_q |\vec{v}_p - \vec{v}_q| d_p}{\mu_q}. \quad (47)$$

$\rho_q$  is the density of the continuous phase,  $\vec{v}_p$  is the velocity of the dispersed phase and  $\vec{v}_q$  is the velocity of the continuous phase.

### 3.1.2 Turbulence

Most engineering CFD topics include a turbulent flow. In some cases, the turbulence can be calculated directly with a very dense computational mesh and time steps, resolving all eddies. This causes a very high computational load, increasing with the Reynolds number approximately proportional to  $Re^3$  (Pope, 2000, 336). Usually direct numerical simulation (DNS) is not practically possible, and a turbulence model is needed.

A turbulence model can be used for all scales of eddies or only for small scale eddies. In large eddy simulations (LES), the conservation equations are filtered not to include small eddies, which are then described with a model. The filtering is done in space, but not in time.

All eddy scales must be modelled when the filtering happens in time. The turbulent fluctuations can be averaged by replacing a variable  $\phi$  with a sum of an average

component  $\bar{\phi}$  and a fluctuating component  $\phi'$ ,

$$\phi = \bar{\phi} + \phi'. \quad (48)$$

When Navier-Stokes equations are averaged, the results are called Reynolds averaged Navier-Stokes (RANS) equations. The fluctuating components are unknown and need to be modelled. In the Reynolds stress model (RSM), there are six conservation equations for Reynolds stresses  $-\rho\overline{u'_i u'_j}$  and one for the turbulence dissipation rate  $\varepsilon$ .

RSM is a quite complex model and uses seven conservation equations, but there are many models with less equations. Most of them use the Boussinesq hypothesis, which gives Reynolds stresses from the mean rates of deformation,

$$-\rho\overline{u'_i u'_j} = \mu_t \left( \frac{\partial u_i}{\partial x_j} + \frac{\partial u_j}{\partial x_i} \right) - \frac{2}{3} \left( \rho k + \mu_t \frac{\partial u_k}{\partial x_k} \right) \delta_{ij}, \quad (49)$$

where  $\mu_t$  is turbulent viscosity and  $k$  is kinetic energy. This way RANS equations can be used with a turbulence model that provides  $k$  and  $\mu_t$ .

The Spalart and Allmaras (1992) model uses only one equation, the transported quantity is  $\tilde{v}$ .

$$\frac{\partial}{\partial t}(\rho\tilde{v}) + \frac{\partial}{\partial x_i}(\rho\tilde{v}u_i) = G_v + \frac{1}{\sigma_{\tilde{v}}} \left[ \frac{\partial}{\partial x_j} \left\{ (\mu + \rho\tilde{v}) \frac{\partial \tilde{v}}{\partial x_j} \right\} + C_{b2}\rho \left( \frac{\partial \tilde{v}}{\partial x_j} \right)^2 \right] - Y_v. \quad (50)$$

Turbulent viscosity is computed as  $\mu_t = \rho\tilde{v}f$ , where  $f$  is a damping function. However, the SA model does not give the turbulent kinetic energy; the  $k$  term in the Boussinesq formula is simply omitted.

The  $k - \varepsilon$  turbulence model (Launder & Spalding, 1974) is probably the most popular turbulence model, it has conservation equations for turbulence kinetic energy  $k$  and energy dissipation rate  $\varepsilon$ .

$$\frac{\partial}{\partial t}(\rho k) + \frac{\partial}{\partial x_i}(\rho k u_i) = \frac{\partial}{\partial x_j} \left[ \left( \mu + \frac{\mu_t}{\sigma_k} \right) \frac{\partial k}{\partial x_j} \right] + G_k + G_b - \rho \varepsilon - Y_M, \quad (51)$$

$$\frac{\partial}{\partial t}(\rho \varepsilon) + \frac{\partial}{\partial x_i}(\rho \varepsilon u_i) = \frac{\partial}{\partial x_j} \left[ \left( \mu + \frac{\mu_t}{\sigma_\varepsilon} \right) \frac{\partial \varepsilon}{\partial x_j} \right] + C_{1\varepsilon} \frac{\varepsilon}{k} (G_k + C_{3\varepsilon} G_b) - C_{2\varepsilon} \rho \frac{\varepsilon^2}{k} + S_\varepsilon, \quad (52)$$

where  $G_k$  and  $G_b$  are turbulence generation terms by mean velocity gradients and by buoyancy, respectively.  $Y_M$  is the effect of compressibility on the turbulence used in Ansys Fluent  $Y_M = 2\rho\varepsilon\sqrt{k/c^2}$ , where  $c$  is the speed of sound.

Turbulent viscosity is a function of  $k$  and  $\varepsilon$

$$\mu_t = \rho C_\mu \frac{k^2}{\varepsilon}. \quad (53)$$

The model includes parameters  $\sigma_k$ ,  $\sigma_\varepsilon$ ,  $C_{1\varepsilon}$ ,  $C_{2\varepsilon}$ ,  $C_{3\varepsilon}$  and  $C_\mu$ . Typically used values are  $\sigma_k=1.0$ ,  $\sigma_\varepsilon=1.3$ ,  $C_{1\varepsilon}=1.44$ ,  $C_{2\varepsilon}=1.92$ ,  $C_{3\varepsilon}=1.0$  and  $C_\mu=0.09$ .

Shih, Liou, Shabbir, Yang, and Zhu (1995) proposed a modification to the standard model

$$\begin{aligned} \frac{\partial}{\partial t}(\rho\varepsilon) + \frac{\partial}{\partial x_j}(\rho\varepsilon u_j) = \frac{\partial}{\partial x_j} \left[ \left( \mu + \frac{\mu_t}{\sigma_\varepsilon} \right) \frac{\partial \varepsilon}{\partial x_j} \right] + \rho C_1 S \varepsilon - \rho C_2 \frac{\varepsilon^2}{k + \sqrt{\nu \varepsilon}} \\ + C_{1\varepsilon} \frac{\varepsilon}{k} C_{3\varepsilon} G_b + S_\varepsilon. \end{aligned} \quad (54)$$

$C_1$  is not a constant but a function of the strain rate,  $C_1 = \max \left[ 0.43, \frac{\eta}{\eta+5} \right]$ , where  $\eta = S \frac{k}{\varepsilon}$ . Turbulent viscosity is as in Equation 53, but  $C_\mu$  is a function not a constant.

In the  $k - \omega$  models two conservation equations are for turbulence kinetic energy and specific dissipation rate  $\omega$ . The standard  $k - \omega$  model by Wilcox (1998) is as follows:

$$\frac{\partial}{\partial t}(\rho k) + \frac{\partial}{\partial x_i}(\rho k u_i) = \frac{\partial}{\partial x_j} \left( \Gamma_k \frac{\partial k}{\partial x_j} \right) + G_k - Y_k + S_k, \quad (55)$$

$$\frac{\partial}{\partial t}(\rho \omega) + \frac{\partial}{\partial x_i}(\rho \omega u_i) = \frac{\partial}{\partial x_j} \left( \Gamma_\omega \frac{\partial \omega}{\partial x_j} \right) + G_\omega - Y_\omega + S_\omega. \quad (56)$$

In both equations,  $G$  equals generation and  $Y$  equals dissipation. These equations are very similar to the  $k - \varepsilon$  model, although the turbulent viscosity is different. Here  $\mu_t = \alpha^* \frac{\rho k}{\omega}$  where the coefficient  $\alpha^*$  enables turbulence dampening for low Re situations. However, the main difference is in the generation and dissipation terms and constants. The specific dissipation dimension equals  $[1/s]$  rather than  $[m^2/s^3]$ , as in  $\varepsilon$  in the  $k - \varepsilon$  model.

There are also hybrid models, such as the  $k - \omega$  shear stress transport ( $k - \omega$  SST) model by Menter (1994), which combines  $k - \omega$  near walls and  $k - \varepsilon$  in the free stream area, combining the strengths of each model.

**Table 2. CFD modelling cases.**

CFD case	Properties	Results
NASA rocket nozzle (Paper III)	Steady-state, axisymmetric 2D, compressible, several turbulence models	Turbulence model for supersonic jet
Single-hole lance (Paper I)	Steady-state, axisymmetric 2D, compressible, modified $k-\varepsilon$	Jet heat transfer rate
Multi-hole lance (Paper I)	Steady-state, 3D, compressible, modified $k-\varepsilon$	Jet heat transfer rate
Subsonic jet impingement (Paper III)	Steady-state, axisymmetric 2D, compressible, modified $k-\varepsilon$	Heat transfer coefficients
CAS-OB lance (Paper II, Paper III)	Steady-state, axisymmetric 2D, compressible, modified $k-\varepsilon$	Heat transfer coefficients
CAS-OB lance with melt (Paper III)	Transient, axisymmetric 2D, compressible, modified $k-\varepsilon$ , VOF multiphase	Melt cavity formation
CAS-OB interior (Paper IV)	Transient, 3D, incompressible, $k-\varepsilon$ , Eulerian multiphase	Ladle interior heat transfer coefficient, melt surface mass transfer coefficient
CAS-OB exterior (Paper IV)	Steady-state, 3D, compressible, $k-\varepsilon$	Bell and ladle exterior heat transfer coefficients

### 3.1.3 *CFD models developed*

CFD simulations were used in several applications in this study and are presented in Table 2. In the following, the most important models are introduced, while more information for the others can be found in the papers.

#### *Turbulence model for supersonic lance, NASA rocket nozzle*

Several turbulence models were tested in this work, most with their recommended parameter settings, but the  $k - \varepsilon$  model was also tested with tuned parameter values. The reason for this was, that the model is a robust two equation model that has been widely tested to give good results compared to the computational effort. The default parameters have been determined to suit many kinds of flow situations and presumably are not optimal for supersonic flow simulations.

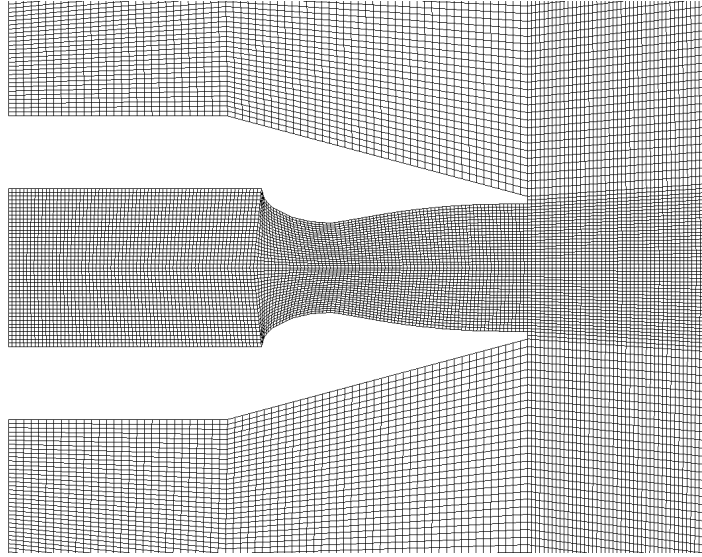


**Fig. 4. Test nozzle geometry.**

The test nozzle geometry was chosen to be a NASA rocket test nozzle (Shoemaker, 1965), because there is experimental data available (Eggers, 1966) and the size of the nozzle is similar to the one in a CAS-OB lance head. The nozzle geometry and a part of the computational mesh is presented in Figure 4 and the whole mesh in Figure 5. The boundaries of the simulation domain can be seen in Figure 6.

The computational domain is a 2D axisymmetric mesh, and the symmetry axis is at the jet centreline. The only wall in the domain is the nozzle surface. The nozzle inlet is a pressure inlet and the other edges are pressure outlets. The inlet pressure is set at 1.18 MPa as in the experiments, the pressure is calculated from the nozzle throat and exit areas (see Equation 8). The outlet pressure was set at atmospheric pressure and all temperatures to room temperature.

In the simulations the flow was calculated with several turbulence models and the  $k - \epsilon$  turbulence model was studied in detail by finding an optimal set of parameters to match experimental data.

### *Supersonic lance CFD modelling*

In metallurgical processes the lance heads are often equipped with multiple nozzles. In order to compare the heat transfer efficiency between a multi-hole lance and a single-hole

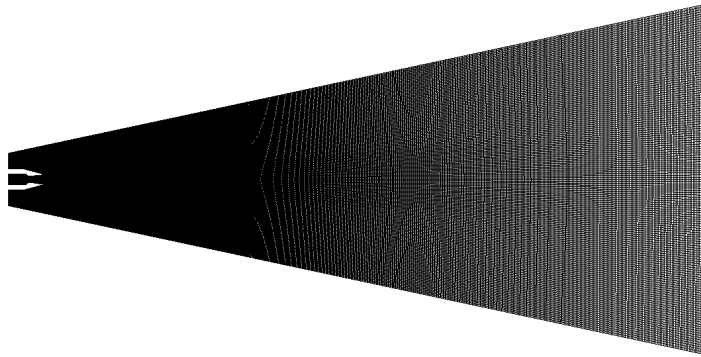


**Fig. 5.** The whole computational mesh, symmetry mirrored.

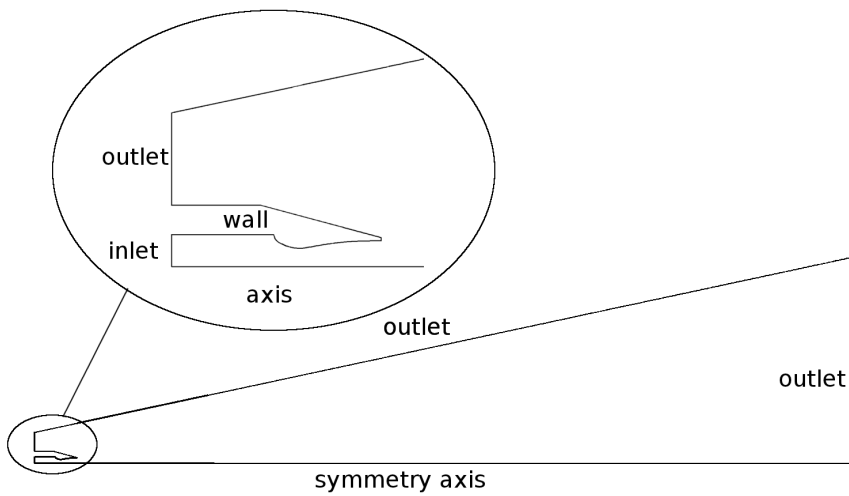


**Fig. 6.** The computational domain and the boundary types.

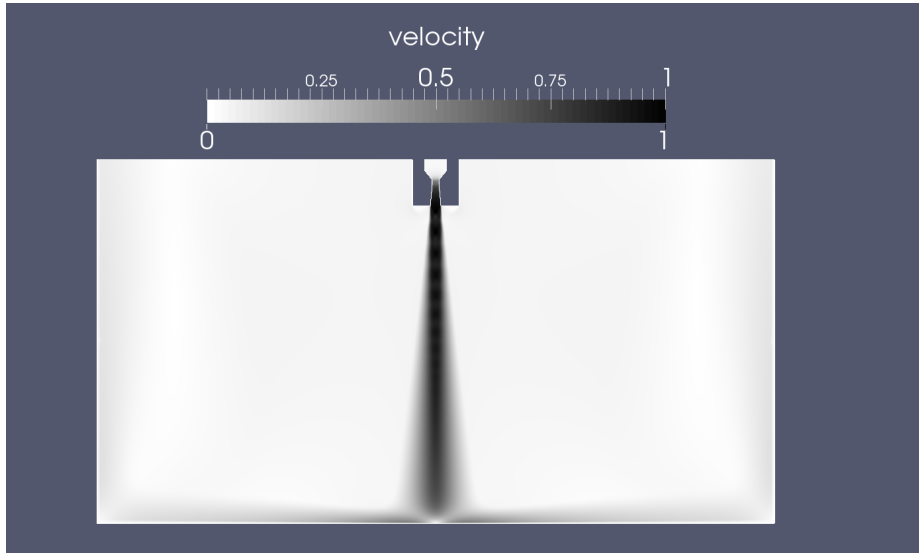


**Fig. 7. Single hole lance simulation domain, symmetry mirrored (modified from Paper I © 2013 Trans Tech Publications).**

lance, two lances of the same mass flow rate design were simulated, one with a single nozzle and another with three nozzles. The computational domains consisted of the lance and a flat wall. The single-hole lance exit diameter was used as a unit of measure in the geometries. The lance height was 60 exit diameters and the flat wall radius 65 exit diameters. The single-hole lance was computed with an axisymmetric mesh, and the multi-hole lance with a 3D mesh of a 1/6 slice of the whole system. The slice contains a half of one nozzle and jet and a half of the space in between the jets. The sliced surfaces were modelled as symmetry planes in the simulation. The computational domain of the single nozzle case is presented in Figure 7 and the three nozzle case in Figures 8 and 9.

The inlet temperature was set to 300 K, the ambient temperature to 1873 K and the flat surface and the side walls to 2000 K. The flat surface mimics the melt and the sides of the refractory walls in steelmaking conditions. The gas feed rate was adjusted to be the same in both cases. The heat transfer coefficient and Nusselt number were calculated in every cell on the flat surface, from the heat flux

$$q = hA(T_s - T_i), Nu = \frac{hl}{\lambda}, \quad (57)$$

where  $T_s$  is the surface temperature and  $T_i$  is lance inlet temperature, and  $\lambda$  is heat conductivity. For comparison of the total heat transfer rate the Nusselt numbers were

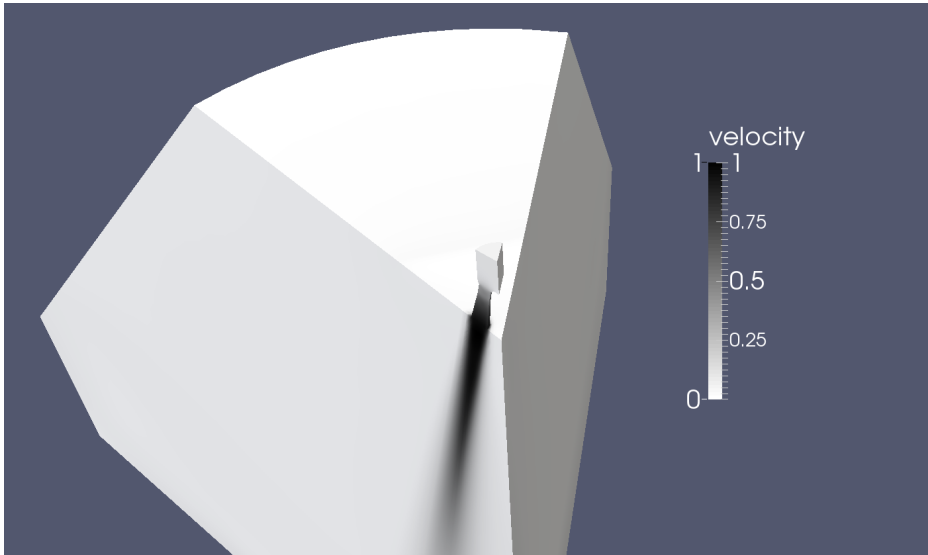


**Fig. 8.** A 1/6 slice domain to model a three nozzle lance.

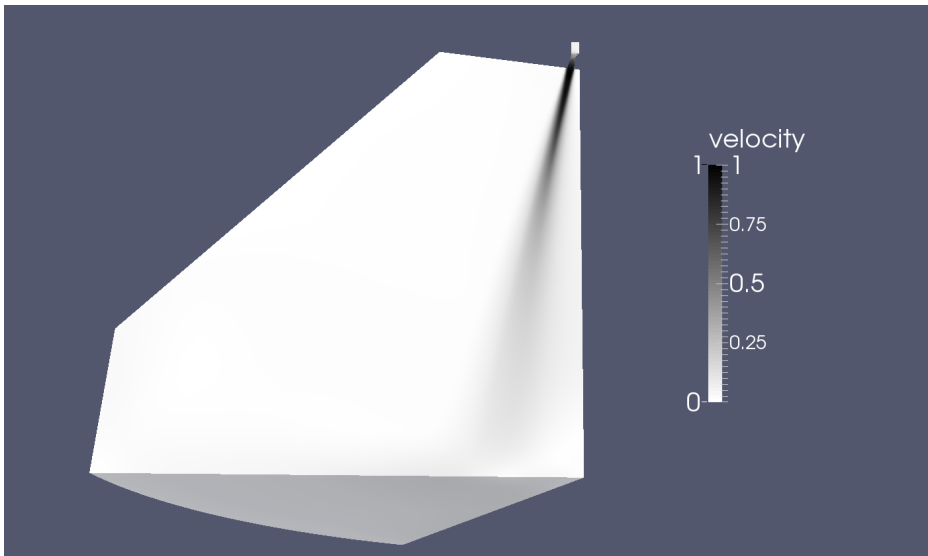


**Fig. 9.** A 1/6 slice domain to model a three nozzle lance, side view.

averaged over the whole surface. A heat and mass transfer analogy can be used to obtain the Sherwood number from the Nusselt number, as has been previously done by Lohe (1966, 1967) in experimental lance studies.

The CAS-OB lance simulations were done in 11 different computational domains to determine how the lance height from the melt surface affects the heat and mass transfer. The range of lance heights is from 1 m to 2 m. An example domain for a lance height of 1.5 m is presented in Figure 10, with the symmetry mirrored. All the geometries can be seen in Figure 11. The bell and melt surface temperatures were set at 2000 K in all cases. It was found that the value of the temperature was not critical for determining the heat transfer coefficients, in the tests between 1500-2500 K the difference in the resulting heat transfer coefficient was found to be less than 2%.

For 11 cases the surface heat transfer coefficients were calculated and the corresponding mass transfer coefficients were found by heat and mass transfer analogy

$$\frac{Sh}{Sc^n} = \frac{Nu}{Pr^n}, n = 0.42. \quad (58)$$

#### *CFD model of the whole CAS-OB*

The Eulerian multiphase model was used in the gas-steel melt multiphase model of the CAS-OB ladle and bell. The phases were modelled so that they were incompressible for easier convergence, therefore special arrangements were made with lance inlet. The oxygen jet velocity profile for the oxygen inlet was calculated from simulation results of the supersonic lance. The data was taken 1 m away from lance head where the compressibility effects are not significant. In the calculation of the new inlet values, the dynamic pressure of the jet was conserved.

The melt surface outside the bell was treated as a wall, while the surface inside the bell which the jet hits was free. The bubble size was set at a constant 0.01 m for argon bottom blowing, which was estimated according to literature (Szekely, Carlsson, & Helle, 1989; Xu, Ersson, & Jönsson, 2015).

The model was used to study the effect of the lance blowing on melt flows and the mass transfer rate in the melt.

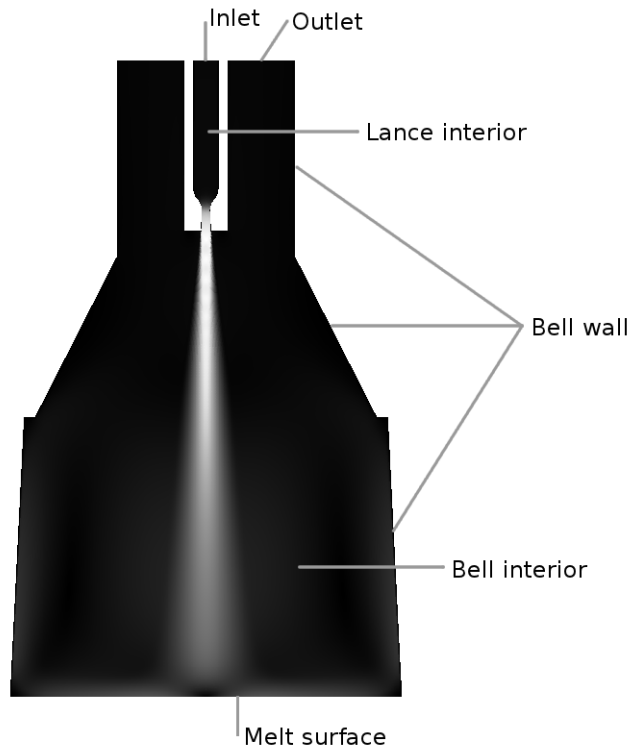


Fig. 10. The parts of the CAS-OB lance CFD model (modified from Paper III © 2015 Wiley-VCH).



Fig. 11. All geometries for CFD modelling, with lance heights from 1 m to 2 m (modified from Paper III © 2015 Wiley-VCH).

### 3.2 CAS-OB heating stage model

In this section the CAS-OB heating stage process model is presented in its final format (Paper IV). The heating stage process model includes a ladle and a bell. The bell is modelled both in lowered and uplifted positions. This principle can be seen in Figure 12. In the upper position the bell interacts with the ladle via heat radiation. During the chemical heating the bell is lowered so that the bell lower wall is submerged in the melt. The modelled phenomena on heating are presented in Figure 13. The main assumptions of the model are:

- Reactions happen on the melt-gas and steel droplet-slag surfaces and in the bulk gas phase.
- Reaction surfaces have no mass.
- Reaction rates are limited by mass transfer only.
- Converter slag is present only outside the bell, which is lowered in an open eye created by argon bubbling.

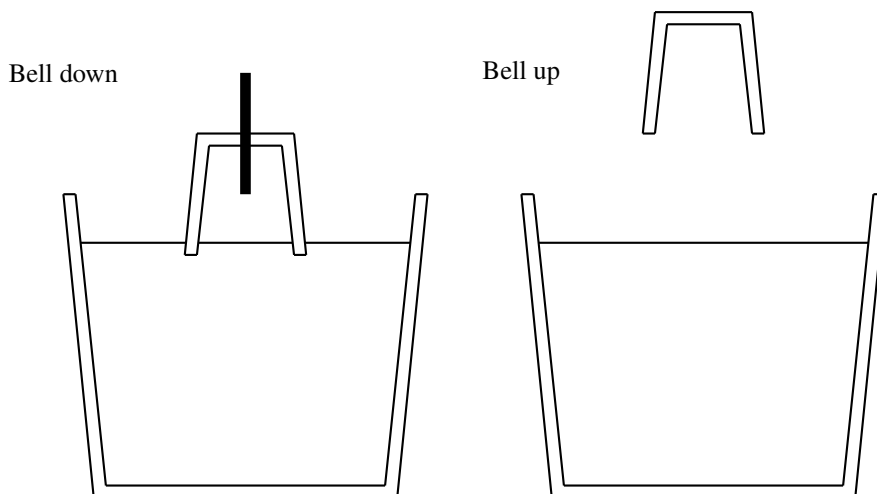


Fig. 12. Model geometries for the CAS-OB heating stage model (modified from Paper IV © 2018 Wiley-VCH).

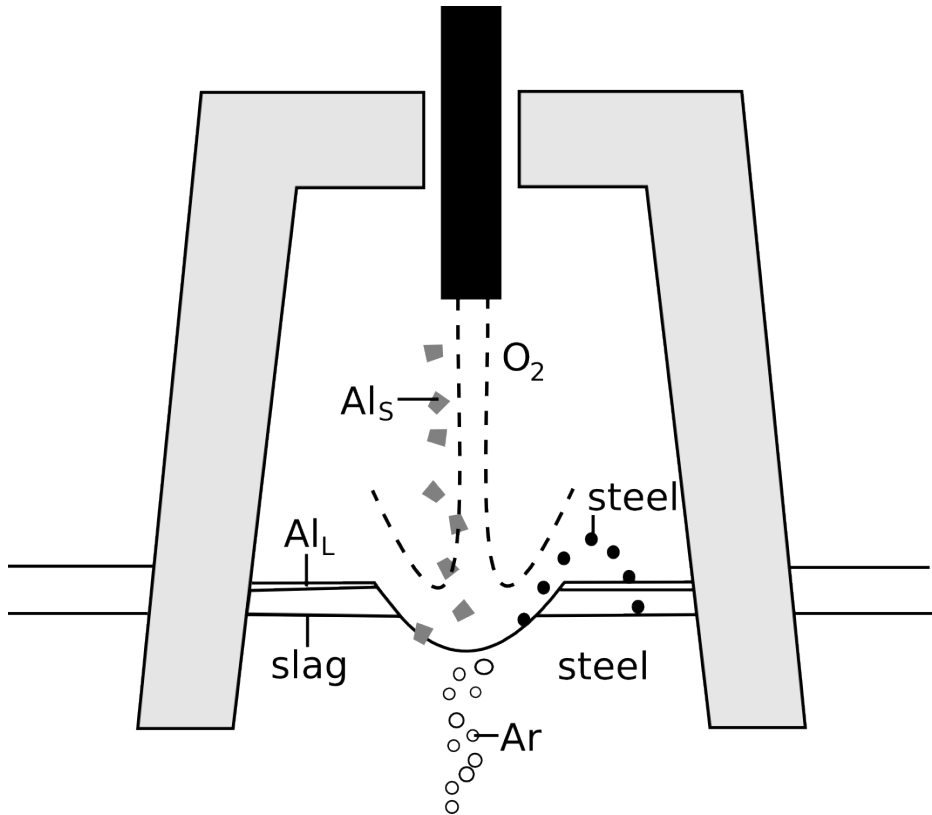
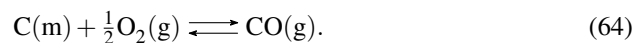
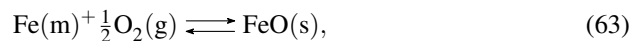
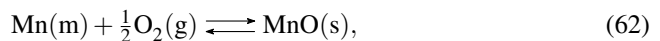
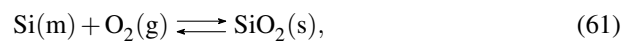
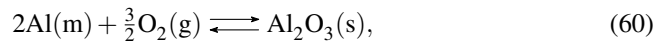
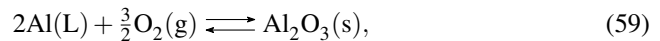


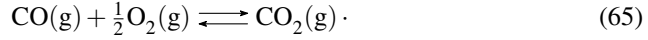
Fig. 13. Schematic description of modelled phases inside the bell (Paper IV © 2018 Wiley-VCH).

### 3.2.1 Reaction system

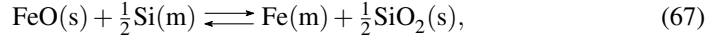
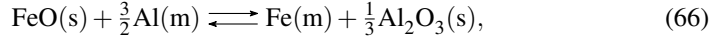
The following reactions are considered in the melt-gas reaction surface:



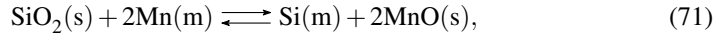
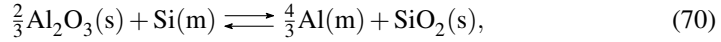
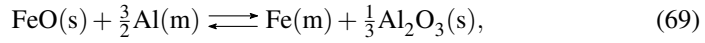
The gas phase has only one reaction:



The reactions of steel droplets in the slag layer are modelled with three reactions



Phases are marked as liquid aluminium (L), slag (s), steel melt (m) and gas (g). The reaction system indirectly takes care of all other possible reactions with the species included by assuming a local chemical equilibrium at the massless reaction surfaces. For example, the reactions 66-68 could have been chosen differently, for instance



but still yielding practically the same results.

The reaction rate for reaction  $i$  is calculated as

$$R_i = k_{f,i} \left( \prod_{re} a_{re}^{v_{re}} - \frac{\prod_{pr} a_{pr}^{v_{pr}}}{K_i} \right). \quad (72)$$

For example the reaction rate for reaction 59 is

$$R = k_f \left( a_{Al}^2 a_{O_2}^{1.5} - \frac{a_{Al_2O_3}}{K_1} \right). \quad (73)$$

The equilibrium constant of a reaction is given by

$$K_i = \exp \left( -\frac{\Delta G_i^\circ}{RT} \right), \quad (74)$$

where  $\Delta G_i^\circ$  is Gibbs free energy change of reaction  $i$ . The Gibbs free energy

$$G^\circ(T) = H^\circ(T) - TS^\circ(T) \quad (75)$$

for each component participating in the reaction is calculated as

$$G^\circ(T) = \Delta H_{T_0}^\circ + \int_{T_0}^T C_p(T) dT - T \left( S_{T_0}^\circ + \int_{T_0}^T \frac{C_p(T)}{T} dT \right), \quad (76)$$

where  $H_{T_0}^\circ$  and  $S_{T_0}^\circ$  are enthalpy and entropy at reference temperature  $T_0$ . The heat capacity  $C_p$  is given by Shomate equation

$$C_p(T) = A + BT + CT^2 + DT^3 + \frac{E}{T^2}. \quad (77)$$

The NIST database (Linstrom & Mallard, 2017) was used for the parameter values  $A$ ,  $B$ ,  $C$ ,  $D$  and  $E$ . MnO data is not available from the NIST database, therefore the HSC database (Outotec, 2015) was used instead using the formula

$$C_p(T) = A + BT + CT^{-2} + DT^2. \quad (78)$$

The activities of the species in steel phase are calculated using Unified Interaction Parameter formalism (UIP) (Pelton & Bale, 1986; Bale & Pelton, 1990), where the activity coefficient  $\gamma_i$  for species  $i$  is defined as

$$\ln\gamma_i = \ln\gamma_i^0 + \ln\gamma_{solvent} + \sum_{j=1}^N \varepsilon_{ij}x_j, \quad (79)$$

where  $\gamma_0$  is the interaction coefficient at an infinite dilution,  $\varepsilon_{ij}$  is the interaction coefficient and  $x_j$  is the mole fraction. The activity coefficient of the solvent is

$$\ln\gamma_{solvent} = -\frac{1}{2} \sum_{j=1}^N \sum_{k=1}^N \varepsilon_{jk}x_jx_k. \quad (80)$$

A quadratic formalism by Ban-Ya (1993) is used for activities for the slag components. The activity of component  $i$  is

$$RT\ln\gamma_i = \sum_{j=1}^N \alpha_{ij}x_j^2 + \sum_{j=1}^N \sum_{k=1}^N (\alpha_{ij} + \alpha_{ik} + \alpha_{jk})x_jx_k + \Delta G_c, \quad (81)$$

where  $\alpha_{ij}$  is interaction energy,  $x_j$  is cation fraction and  $\Delta G_c$  is the conversion factor between the regular solution and the real solution. The ideal gas law is used for gas phase activities.

A reaction quotient is used in the determination of equilibrium

$$Q = \frac{\prod_i a_i^{v_i}}{\prod_j a_j^{v_j}}, \quad (82)$$

where  $i$  represents the products,  $j$  the reactants and  $v$  is the stoichiometric coefficient. At equilibrium  $Q$  equals the equilibrium constant  $K$ . During the calculation the ratio  $K/Q$  is monitored, and the forward rate coefficient  $k_f$  is increased until the ratio is close to unity.

### 3.2.2 Mass transfer

The diameter  $d_f$  and depth  $H_f$  of the depression caused by the lance jet are calculated according to the correlation by Koria and Lange (1987), where

$$d_f = 2.813H\dot{M}^{0.282} \quad (83)$$

and

$$H_f = 4.469H\dot{M}^{0.66}. \quad (84)$$

$\dot{M}$  is dimensionless momentum flux, calculated as

$$\dot{M} = \frac{\dot{V}_g \rho_g u_j}{\rho_l g H^3}, \quad (85)$$

where  $\dot{V}_g$  is the volume flux and  $\rho_g$  is the gas density, both in NTP conditions.  $\rho_l$  is the melt density and  $g$  is the gravitational acceleration.

Spherical cap geometry is assumed in calculating the surface area of the cavity  $A_f$

$$A_f = \pi \left( \frac{d_f^2}{2} + H_f^2 \right). \quad (86)$$

The supersonic jet causes steel droplets to detach from the melt surface, the droplet generation rate is calculated by a model by Rout, Brooks, Subagyo, Rhamdhani, and Li (2016) which is a modified version of model by Subagyo, Brooks, Coley, and Irons (2003).

$$R_B = \frac{F_g N_B^{3.2}}{(2.6 \times 10^6 + 2.0 \times 10^{-4} N_B^{12})^{0.2}}, \quad (87)$$

where  $F_g$  is volumetric gas flow rate at the process temperature and pressure.  $N_B$  is blowing number

$$N_B = \frac{\eta^2 \rho_g u_j^2}{2\sqrt{\rho_l \sigma_l g}}, \quad (88)$$

where  $\eta$  is a parameter,  $u_j$  is the axial velocity of the jet and  $\sigma_l$  is the surface tension of the melt. The droplets are assumed to fall through the slag layer at terminal velocity, given by (Brooks, Pan, Subagyo, & Coley, 2005)

$$u_d = 0.153 \left( \frac{d_d g (\rho_M - \rho_s)}{\rho_s} \left( \frac{d_d \rho_s}{\mu_s} \right)^{0.6} \right)^{1/1.4}, \quad (89)$$

**Table 3. Diffusion coefficients in steel melt, m/s<sup>2</sup> (Kawai, Shiraishi, Kyōkai, & 140th Committee, 1988).**

Al	C	Mn	Ni	Si	Fe
$3.5 \times 10^{-9}$	$1 \times 10^{-8}$	$4.96 \times 10^{-9}$	$4.83 \times 10^{-9}$	$6 \times 10^{-7}$	$4 \times 10^{-9}$

where  $d_d$  is the droplet diameter. The mass of the droplets in the slag layer is given by

$$m_d = \min(\tau_d, t)R_B, \quad (90)$$

where  $t$  is the lance blowing time and  $\tau_d = \frac{H_s}{u_d}$ . The surface area of the droplets is important for reaction modelling and is calculated from droplet mass as

$$A_d = \frac{6m_d}{d_d\rho_l}. \quad (91)$$

The penetration model by Higbie (1935), is used for the mass transfer inside the steel droplets, where

$$h_{i,d} = 2\sqrt{\frac{D_i}{\pi d_d/u_d}}. \quad (92)$$

The steel melt mass transfer was calculated according to the correlation proposed by Kataoka and Miyauchi (1969)

$$h_i = c \left( \frac{\varepsilon}{\nu} \right)^{\frac{1}{4}} D_i^{\frac{1}{2}}, \quad (93)$$

where  $\nu$  is the kinematic viscosity. The constant  $C$  was 0.3, in the literature (Kataoka & Miyauchi, 1969; Laakkonen, Alopaeus, & Aittamaa, 2006; Venturini & Goldschmit, 2007) values of 0.3 and 0.5 were used. The turbulence dissipation rate  $\varepsilon$  was obtained from a CFD simulation of the whole CAS-OB. Diffusion coefficients  $D_i$  in the steel are given in Table 3.

In the model, aluminium particles are dropped onto the melt surface, where they float, dissolve and melt. A fraction of 0.42 of the surface is in the liquid steel because of buoyancy. The aluminium dissolution into the steel is determined by mass transfer, calculated by the Ranz-Marshall correlation (Bird, Stewart, & Lightfoot, 1960)

$$Sh = 2 + 0.6Re^{0.5} Sc_{Al}^{1/3}. \quad (94)$$

The melting time of aluminium is solved analytically, yielding

$$\tau_m = \frac{d_{AL}^2 \rho_{Al} l_m}{8\lambda_e (T - T_m)}, \quad (95)$$

where  $l_m$  is the melting heat of aluminium,  $\lambda_e$  is effective conductivity and  $T_m$  is the aluminium melting temperature. The liquid aluminium is assumed to immediately be blown to the top of the slag layer, out of the free melt surface in the cavity.

Other heat and mass transfer correlations were determined by means of CFD simulations and are given in section 4.1.3.

### 3.2.3 Radiation heat transfer

A very important phenomena in high temperature heat transfer is thermal radiation. In the first version (Paper II) of the heating stage process model, radiation was taken into account only inside the bell where the view factors can be calculated by reciprocity relation  $A_i F_{ij} = A_j F_{ji}$  (Incropera & De Witt, 1985, 626). In the second version (Paper IV), radiation heat transfer was applied to all radiating surfaces. Since the geometry is quite complex, the additional view factors were acquired from Ansys Fluent CFD cases.

The radiosities  $J$  of different surfaces affect each other, therefore radiation balance equations were solved implicitly together with other heat transfer conservation equations. The radiation conservation equation for each surface  $i$  is (Incropera & De Witt, 1985, 640)

$$\frac{E_{bi} - J_i}{(1 - \varepsilon_i)/\varepsilon_i A_i} = \sum_{j=1}^N \frac{J_i - J_j}{(A_i F_{ij})^{-1}}, \quad (96)$$

where  $E_{bi}$  is black body radiation from surface  $i$  and  $F_{ij}$  is the view factor from surface  $i$  to surface  $j$ .

### 3.2.4 Mass conservation

At the reaction surfaces the mass conservation equations take the following form

$$h\rho\Delta y + \dot{m}y = \sum v^* R_{surface}, \quad (97)$$

where  $h$  is the mass transfer coefficient,  $y$  is the mass fraction,  $\dot{m}$  is the total mass flow rate from all reactions and  $R_{surface}$  is the reaction rate at the reaction surface. This means that the mass transfer rate equals the total reaction rate of a given species. The surfaces are assumed to be infinitely thin and massless, therefore there is no storage term in the equations. In bulk phases a storage term is added, and the basic form is

$$h\rho\Delta y + \dot{m}y = \sum v^* R_{bulk} - V\rho \frac{dy}{dt}. \quad (98)$$

Depending on the conserved entity, some source and sink terms are added if needed. These include gas and aluminium feeds into the system and links from one conservation equation to another for example when solid aluminium melts.

For clarity, the Stefan flow terms are marked with  $B(\dot{m}, i)$ , for example, the oxygen transfer due bulk flow between free melt surface and gas phase is

$$B(\dot{m}_{g,f}, O_2) = \max(\dot{m}_{g,f}, 0)y_{O_2} - \max(-\dot{m}_{g,f}, 0)y_{O_2f}, \quad (99)$$

where  $\dot{m}_g$  is the mass flow caused by all reactions at the reaction surface,  $y_{O_2}$  is the oxygen mass fraction in the bulk gas and is the  $y_{O_2f}$  oxygen mass fraction at the reaction surface.

A list of mass conservation equations is as follows. The oxygen conservation equation at the free melt surface:

$$h_{O_2,f}\rho_g(y_{O_2} - y_{O_2f}) + B(\dot{m}_{g,f}, O_2) = -\sum_{i=2}^6 v_{i,O_2}^* R_i. \quad (100)$$

Oxygen on the pure aluminium surface:

$$h_{O_2,Al}\rho_{g,Al}(y_{O_2} - y_{O_2,Al}) + B(\dot{m}_{g,Al}, O_2) = -R_1 v_{1,O_2}^*. \quad (101)$$

Oxygen in bulk gas:

$$\begin{aligned} \dot{m}_{O_2,in} - \dot{m}_{g,out}y_{O_2} + R_7V_g v_{7,CO}^* - h_{O_2,f}A_f\rho_{g,f}(y_{O_2} - y_{O_2,f}) - B(\dot{m}_{g,f}, O_2)A_f \\ - h_{O_2,Al}A_{Al}\rho_{g,Al}(y_{O_2} - y_{O_2,Al}) - B(\dot{m}_{g,Al}, O_2)A_{Al} = V_g \frac{d(\rho_g y_{O_2})}{dt}. \end{aligned} \quad (102)$$

$A_f$  is the free surface area, the area of the lance jet cavity.  $A_{Al}$  is area of the pure aluminium layer. Carbon monoxide in bulk gas:

$$\begin{aligned} -\dot{m}_{g,out}y_{CO} - h_{CO,f}A_f\rho_{g,f}(y_{CO} - y_{CO,f}) - B(\dot{m}_{g,f}, CO)A_f \\ + R_7V_g v_{7,CO}^* = V_g \frac{d(\rho_g y_{CO})}{dt}. \end{aligned} \quad (103)$$

Carbon monoxide at the melt surface:

$$h_{CO}\rho_{g,f}(y_{CO} - y_{CO,f}) + B(\dot{m}_{g,f}, CO) = -R_6 v_{6,CO}^*. \quad (104)$$

Carbon dioxide in gas:

$$\begin{aligned} -\dot{m}_{g,out}y_{CO_2} - h_{CO_2,f}A_f\rho_{g,f}(y_{CO_2} - y_{CO_2,f}) \\ + B(\dot{m}_{g,f}, CO_2) + R_7V_g v_{7,CO_2}^* = V_g \frac{d(\rho_g y_{CO_2})}{dt}. \end{aligned} \quad (105)$$

Carbon dioxide at melt surface:

$$h_{CO_2,f}\rho_{g,f}(y_{CO_2} - y_{CO_2,f}) = B(\dot{m}_{g,f}, CO_2). \quad (106)$$

Argon at the melt surface:

$$y_{O_2,f} + y_{CO,f} + y_{CO_2,f} + y_{Ar,f} = 1.0. \quad (107)$$

Argon in gas:

$$y_{O_2} + y_{CO} + y_{CO_2} + y_{Ar} = 1.0. \quad (108)$$

Mass of solid aluminium  $m_{Al,S}$ :

$$\dot{m}_{Al,S} - m_{Al,S}R_{melt} = \frac{dm_{Al,S}}{dt}. \quad (109)$$

$R_{melt}$  is the melting rate of solid aluminium. Liquid pure aluminium:

$$m_{Al,S}R_{melt} + h_{Al,L}A_d(y_{Al,d} - 1.0) + h_{Al,S}A_{Al,S}\rho_l(y_{Al} - 1.0) + v_{1,Al}^*A_{Al}R_1 = \frac{dm_{Al,l}}{dt}. \quad (110)$$

$A_d$  is area of steel droplets in the slag. Aluminium in the steel melt:

$$\begin{aligned} & -h_{Al}A_f\rho_l(y_{Al} - y_{Al,f}) - B(\dot{m}_l, Al)A_f \\ & -h_{Al,d}A_d\rho_l(y_{Al} - y_{Al,d}) - B(\dot{m}_{l,d}, Al)A_d \\ & -h_{Al,S}A_{Al,S}\rho_l(y_{Al} - 1.0) = \frac{d(m_l y_{Al})}{dt}. \end{aligned} \quad (111)$$

Aluminium at the melt surface:

$$h_{Al}\rho_l(y_{Al} - y_{Al,f}) + B(\dot{m}_l, Al) = -R_2 v_{2,Al}^*. \quad (112)$$

Aluminium at the steel droplet surface:

$$h_{Al,L}A_d(1.0 - y_{Al,d}) + h_{Al,d}\rho_l(y_{Al} - y_{Al,d}) + B(\dot{m}_{l,d}, Al) = -R_8 v_{8,Al}^*. \quad (113)$$

Silicon in steel melt:

$$\begin{aligned} & -h_{Si}A_f\rho_l(y_{Si} - y_{Si,f}) - B(\dot{m}_l, Si)A_f - h_{Si,d}A_d\rho_l(y_{Si} - y_{Si,d}) \\ & - B(\dot{m}_{l,d}, Si)A_d = \frac{d(m_l y_{Si})}{dt}. \end{aligned} \quad (114)$$

Silicon at the melt surface:

$$h_{Si} \rho_l (y_{Si} - y_{Si,f}) + B(\dot{m}_l, Si) = -R_3 v_{3,Si}^* \quad (115)$$

Silicon at the steel droplet surface:

$$h_{Si,d} \rho_l (y_{Si} - y_{Si,d}) + B(\dot{m}_{l,d}, Si) = -R_9 v_{9,Si}^* \quad (116)$$

Steel melt mass conservation equation:

$$\begin{aligned} & -h_{Al,S} A_{Al,S} \rho_l (y_{Al} - 1.0) \\ & - \sum_{i=1}^6 (h_i A_f \rho_l (y_i - y_{i,s}) - B(\dot{m}_l, i) A_f) \\ & - \sum_{i=1}^5 (h_{i,d} A_d \rho_l (y_i - y_{i,d}) - B(\dot{m}_{l,d}, i) A_d) = \frac{dm_l}{dt} \end{aligned} \quad (117)$$

Aluminium oxide in slag:

$$R_1 A_{Al} v_{1,Al_2O_3}^* + R_2 A_f v_{2,Al_2O_3}^* + R_8 A_d v_{8,Al_2O_3}^* = -\frac{d(m_s y_{Al_2O_3})}{dt} \quad (118)$$

Slag mass conservation:

$$\begin{aligned} & R_1 A_{Al} v_{1,Al_2O_3}^* + R_2 A_f v_{2,Al_2O_3}^* + R_3 A_f v_{3,SiO_2}^* + R_4 A_f v_{4,MnO}^* \\ & + R_5 A_f v_{5,FeO}^* + R_8 A_d v_{8,Al_2O_3}^* + R_8 A_d v_{8,FeO}^* + R_9 A_d v_{9,SiO_2}^* \\ & + R_9 A_d v_{9,FeO}^* + R_{10} A_d v_{10,MnO}^* + R_{10} A_d v_{10,FeO}^* = -\frac{dm_s}{dt} \end{aligned} \quad (119)$$

### 3.2.5 Energy conservation

A list of energy conservation equations is as follows. Massless free surface:

$$\begin{aligned} & \alpha_{l,f} (T_l - T_f) + \alpha_{g,f} (T_g - T_f) - (J_f - J_{B1}) \\ & + \sum_k^n \sum_{i=0}^{n_l+n_g} \max(-R_k v_{i,k}^*, 0) C_{p,i} (T_{g/l} - T_f) = \sum_k^n R_k \Delta h_k (T_f) \end{aligned} \quad (120)$$

$\alpha_{g,f}$  and  $\alpha_{l,f}$  are the heat transfer coefficients for gas and liquid steel, and  $T_{g/l}$  is the temperature of either gas or steel, depending on the phase of species  $i$ . Slag and liquid

aluminium inside the bell:

$$\begin{aligned} & \frac{dm_{Al,l}}{dt} c_{p,Al,l} (T_l - T_o) + \alpha_{l,o} A_o (T_l - T_o) + \alpha_{g,o} A_o (T_g - T_o) - A_o (J_o - J_{B1}) \\ & + \sum_{i=0}^{n_l} R_d y_i c_{p,i} (T_l - T_o) \eta_d - \sum_{k=7}^{10} R_k A_d \Delta h_k (T_o) + \sum_{i=0}^{n_s} \sum_{k=1}^7 R_k v_{k,i}^* A_f c_{p,i} (T_f - T_o) \\ & - \lambda_a A_{B1,o} (T_o - T_{B1}) / (0.5 d_a) = (m_{Al,l} c_{p,Al,l} + m_s c_{p,s}) \frac{dT_o}{dt}. \quad (121) \end{aligned}$$

$A_o$  is the occupied surface area, i.e. the area inside the bell covered with slag or liquid aluminium.  $\eta$  is heat transfer efficiency,  $\eta = 1 - \exp\left(-\frac{6\alpha_d \tau_d}{d_d c_{p,i} \rho_i}\right)$ . The gas space inside the bell:

$$\begin{aligned} & \dot{m}_{O_2,in} c_{p,O_2,in} (T_{O_2,in} - T_g) + \dot{m}_{Ar,in} c_{p,Ar} (T_f - T_g) \\ & - R_6 v_{6,CO}^* A_f c_{p,CO} (T_g - T_f) - \alpha_{g,o} A_{Al} (T_g - T_o) \\ & - \alpha_g A_f (T_g - T_f) - \alpha_{B1} A_{B1} (T_g - T_{B1}) = m_g c_{p,g} \frac{dT_g}{dt}. \quad (122) \end{aligned}$$

The steel melt:

$$\begin{aligned} & \dot{m}_{Ar,in} c_{p,Ar} (T_{Ar,in} - T_l) - \frac{m_{Al,s}}{\tau_m} \left( c_{p,Al,s} (T_{Al,melt} - T_{Al,in}) + l_m (T_{Al,melt}) + c_{p,Al,l} (T_{Al,melt}) \right) \\ & - \alpha_{l,o} A_o (T_l - T_o) - \alpha_{l,f} A_f (T_l - T_f) - \alpha_{l,L} A_{L1} (T_l - T_{L1}) - \alpha_{l,S1} A_{S1} (T_l - T_{S1}) \\ & - \lambda_a A_{B1,sub} (T_l - T_{B1}) / (0.5 d_a) - \lambda_{brick} A_{B2,sub} (T_l - T_{B2}) / (0.5 H_{B2}) \\ & + \sum_{k=2}^6 \left( -\max(-R_k, 0) v_{k,k}^* A_f c_{p,k} (T_f - T_l) \right) \\ & + \sum_{i=0}^{n_l} \left( \max \left( R_d y_i + \sum_{k=7}^{10} (R_k v_{k,i}^*) A_d, 0 \right) \right) c_{p,i} (T_o - T_l) \eta_d = m_l c_{p,L} \frac{dT_l}{dt}. \quad (123) \end{aligned}$$

$A_{L1}$  is the surface area between the steel melt and the ladle and  $A_{S1}$  is the surface area of the slag layer outside the bell.  $\lambda_a$  is the heat conductivity of the material attached to bell interior wall and  $d_a$  is its thickness. Node  $L_1$ , the inner surface of the ladle:

$$\alpha_{l,L} (T_l - T_{L1}) = \lambda_{brick} (T_{L1} - T_{L2}) / (0.5 dx_{Lb}). \quad (124)$$

$dx_{Lb}$  is the thickness of the brick layer in the ladle wall. Node  $L_2$  inside the ladle brick layer:

$$\begin{aligned} & \lambda_{brick} A_{L2} (T_{L1} - T_{L2}) / (0.5 dx_{Lb}) - \lambda_{brick} A_{L2} (T_{L2} - T_{L3}) / (0.5 dx_{Lb}) \\ & - (E_{b,T_{L2}} - J_L) \epsilon_{brick} A_{L,rad} / (1 - \epsilon_{brick}) = m_{brick,L} c_{p,brick} \frac{dT_{L1}}{dt}. \quad (125) \end{aligned}$$

Node  $L_3$ , in between the ladle brick layer and the steel mantle:

$$\lambda_{brick}A_{L4}(T_{L2} - T_{L3})/(0.5dx_{Lb}) - \lambda_{steel}A_{L4}(T_{L3} - T_{L4})/(0.5dx_{Ls}). \quad (126)$$

Node  $L_4$ , the outer surface of the ladle:

$$\begin{aligned} \lambda_{steel}A_{L4}(T_{L3} - T_{L4})/(0.5dx_{Ls}) - \alpha_{L4}A_{L4}(T_{L4} - T_{atm}) \\ - \varepsilon_{steel}A_{L4}\sigma(T_{L4}^4 - T_{atm}^4) = m_{steel,L}c_{p,steel} \frac{dT_{L4}}{dt}. \end{aligned} \quad (127)$$

The inner surface of the bell:

$$\begin{aligned} \alpha_{B1}A_{B1}(T_g - T_{B1}) + A_o(J_o - J_{B1}) + A_f(J_f - J_{B1}) \\ + \lambda_a A_{B1,sub}(T_l - T_{B1})/(0.5d_a) + \lambda_a A_{B1,o}(T_o - T_{B1})/(0.5d_a) \\ - \lambda_{brick}A_{B1}(T_{B1} - T_{B2})/(0.5dx_{Bb}) - A_{B1}d_a\rho_a c_{p,a} \frac{dT_{B1}}{dt}. \end{aligned} \quad (128)$$

Bell wall node 2:

$$\begin{aligned} \lambda_{brick}A_{B1}(T_{B1} - T_{B2})/(0.5dx_{Bb}) - \lambda_{brick}A_{B2}(T_{B2} - T_{B3})/(0.5dx_{Bb}) \\ + \lambda_{brick}A_{B2,sub}l_{bell}(T_l - T_{B2})/(0.5H_{B2}) = m_{brick,B}c_{p,brick} \frac{dT_{B2}}{dt}. \end{aligned} \quad (129)$$

Bell wall node 3:

$$\lambda_{brick}A_{B2}(T_{B2} - T_{B3})/(0.5dx_{Bb}) = \lambda_{steel}A_{B3}(T_{L3} - T_{L4})/(0.5dx_{Bs}). \quad (130)$$

The outer surface of the bell:

$$\begin{aligned} \lambda_{steel}A_{B4}(T_{B3} - T_{B4})/dx_{Bs} - \alpha_{B4}A_{B4}(T_{B4} - T_{atm}) \\ - (E_{b,T_{B4}} - J_{B4})\varepsilon_{steel}A_{B4}/(1 - \varepsilon_{steel}) = m_{steel,B}c_{p,steel} \frac{dT_{B4}}{dt}. \end{aligned} \quad (131)$$

The lower surface of slag layer outside the bell:

$$\alpha_{l,o}(T_l - T_{S1}) = \alpha_s(T_{S1} - T_{S2})/H_{slag}. \quad (132)$$

The upper surface of slag layer:

$$\alpha_s(T_{S1} - T_{S2})/H_{slag} = (E_{b,T_{S2}} - J_{S2})\varepsilon_{slag}/(1 - \varepsilon_{slag}). \quad (133)$$

Energy conservation is not solved simultaneously through the reactions and mass transfer, and in the iteration sequence the energy conservation system is calculated after the mass conservation system. A flow chart of the model is presented in Figure 14.

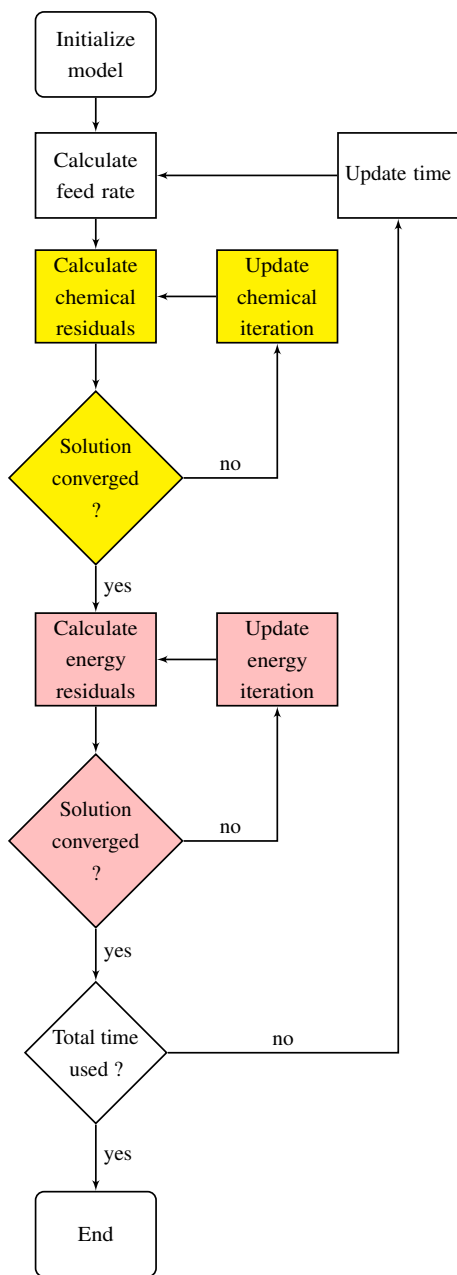


Fig. 14. Flow chart of the CAS-OB heating stage process model (Paper IV © 2018 Wiley-VCH).

### 3.3 Validation measurements

Industrial measurements were taken for model validation. The measurements were conducted on two occasions, in January 2014 and April 2015, at the SSAB Europe steel plant in Raahe, Finland. The experiments are presented in Table 4. The steel and slag samples were taken before and after the heating stage, except in the first measurement campaign in which the steel samples were taken later after the slag reduction stage. Temperature measurements were taken before and after heating, and also in the end of the process so that cooling after heating could be studied too. A thermal camera and pyrometer were used to measure the bell and ladle surface temperatures, and a gas analyser was used for exhaust gas analysis.

The XRF analysis of slag samples does not output MnO and FeO contents, but it shows the Mn and Fe content of the slag. The MnO and FeO content is calculated assuming that all the detected Fe is in FeO, and that all the Mn is in MnO and the analysed metal mass fraction is correct. The FeO and MnO mass fractions are calculated by scaling the measured metal content with the ratio of molar masses, for example the MnO mass fraction is given by

$$y_{MnO} = \frac{y_{Mn}M_{MnO}}{M_{Mn}}. \quad (134)$$

The same is done for FeO. Then all the slag species are scaled to yield the sum of unity,

$$y_i = \frac{y_{i,old}}{\sum y_i}. \quad (135)$$

**Table 4. Measurements at the steel plant.**

Topic	Equipment	Note
Steel composition	sample+OES	2 samples
Slag composition	sample+XRF	2 samples
Melt temperature	probe	3 measurements
Exterior bell temperature	Optris PI120	thermal camera
Interior bell temperature	DIAS Pyrospot DSR10N	pyrometer
Exterior ladle temperature	Optris PI120	thermal camera
Gas analysis	Siemens Ultramat 23-7MB2335	gas analyser

## 4 Results and discussion

In this chapter the results of this thesis are presented and their meaning is discussed.

### 4.1 CFD results

#### 4.1.1 Turbulence model tests

Several turbulence models were tested using the nozzle geometry and experimental data by Eggers (1966). The axial velocity profiles of the jet calculated with different turbulence models are presented in Figure 15, and the corresponding radial velocity profiled at a distance of 1.5 m from the nozzle exit is shown in Figure 16. From the results it was noted that the RSM and SAS models provide the best results, but none of the models accurately matches the experiments. Therefore, it was decided to fit the parameters of the turbulence model to fit the experiments in this case. The well tested standard  $k - \varepsilon$  was chosen as a base model. A good fit was obtained with parameter values  $\sigma_k=0.85$ ,  $\sigma_\varepsilon=0.85$ ,  $C_{1\varepsilon}=1.44$ ,  $C_{2\varepsilon}=1.85$ ,  $C_{3\varepsilon}=0.85$  and  $C_\mu=0.09$ , while the usually used values are  $\sigma_k=1.0$ ,  $\sigma_\varepsilon=1.3$ ,  $C_{1\varepsilon}=1.44$ ,  $C_{2\varepsilon}=1.92$ ,  $C_{3\varepsilon}=1.0$  and  $C_\mu=0.09$ . The results with  $k - \varepsilon$  with modified parameters are presented in Figures 17 and 18, and the entire jet can be seen as a velocity presentation in Figure 19. The static temperature of the jet is presented in Figure 20, while the total temperature is nearly constant. The total temperature includes the motion of the gas in the flow direction. The Mach number in the de Laval nozzle is presented in Figure 21. The number is one at the throat.

Based on the results, the parameter fitted  $k - \varepsilon$  model is used in all the supersonic lance calculations.

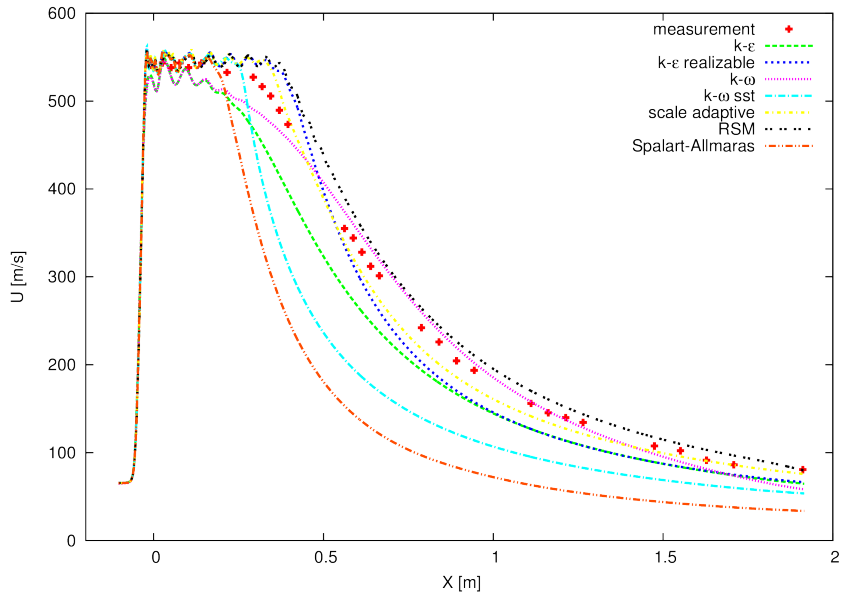


**Fig. 15. Axial velocity of the jet calculated with different turbulence models (modified from Paper III © 2015 Wiley-VCH).**

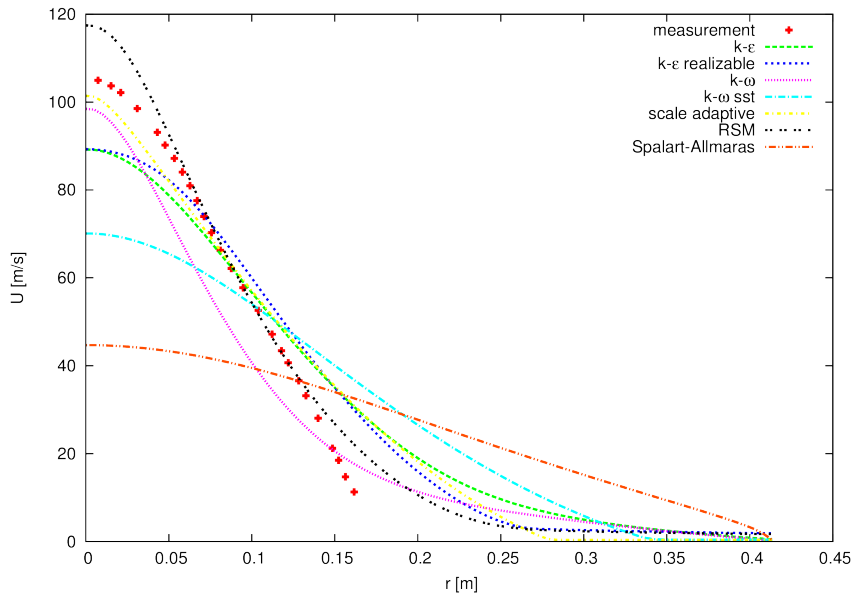


**Fig. 16. Radial velocity of the jet at 1.5m distance from the nozzle (modified from Paper III © 2015 Wiley-VCH).**

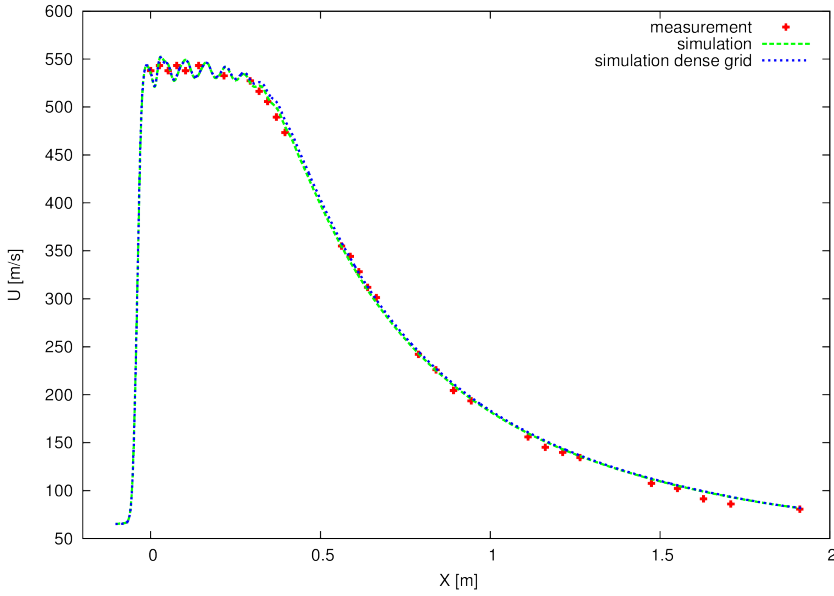


**Fig. 17. Axial velocity of the jet calculated with the modified  $k-\epsilon$  model (Paper III © 2015 Wiley-VCH).**

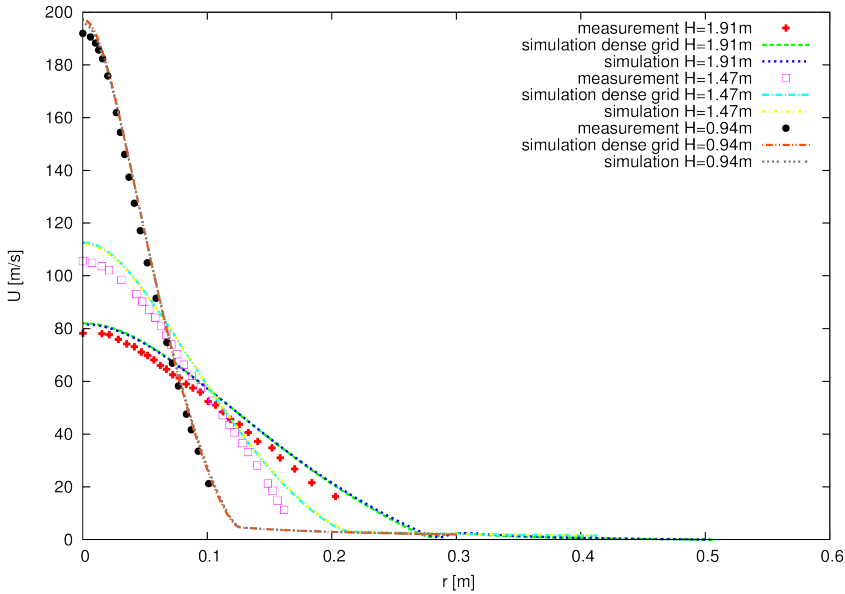


**Fig. 18. Radial velocity of the jet at three different distances, with the modified  $k-\epsilon$  model (Paper III © 2015 Wiley-VCH).**

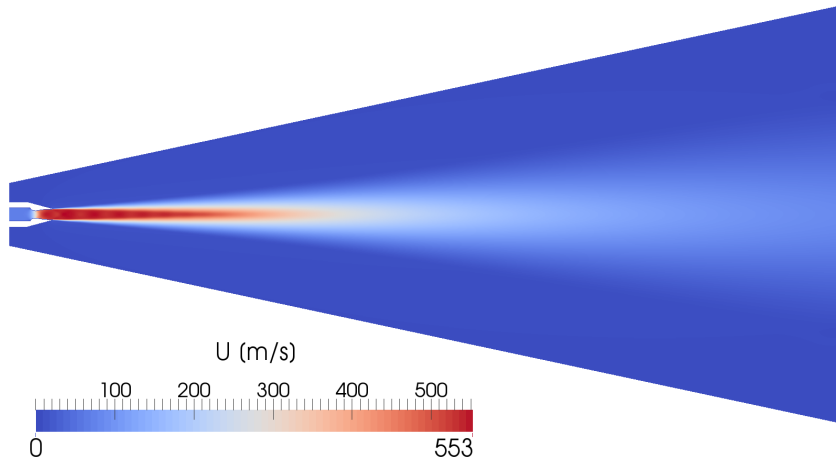


**Fig. 19.** Test case flow velocity, with the modified  $k-\varepsilon$  model (modified from Paper III © 2015 Wiley-VCH).

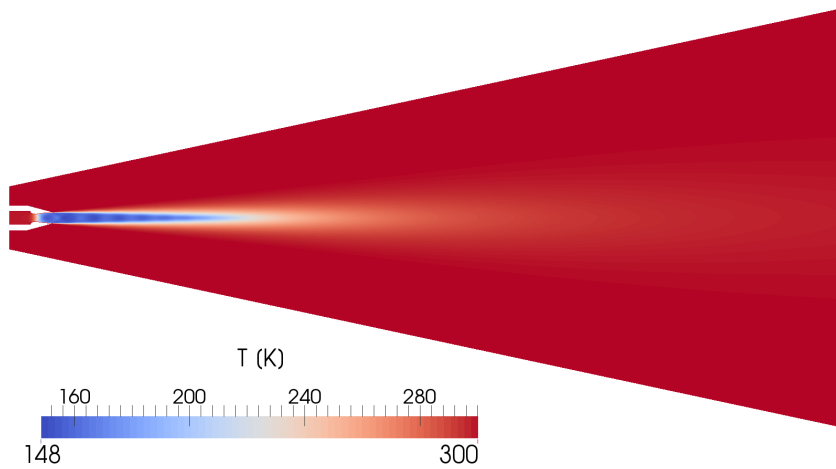


**Fig. 20.** Test case static temperature, with the modified  $k-\varepsilon$  model.

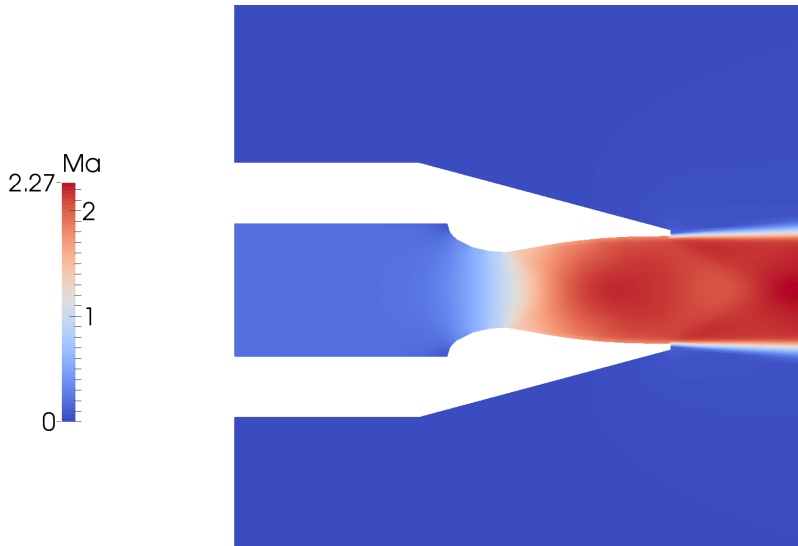


**Fig. 21. Test case Mach number in the nozzle, with the modified  $k-\epsilon$  model.**

#### **4.1.2 *Supersonic lance***

Supersonic lances were studied with three different geometries. One single hole and one multi-hole lance were used in and AOD converter with a CAS-OB lance. The two AOD converter lances are designed for the same mass flow rate and therefore it is interesting to compare the results. As seen in Figure 22 the jets in the multi-hole lance are bent towards each other. In order to plot the jet centreline velocity a user defined function (UDF) was used in Fluent to detect the centreline of an individual jet. The centre is assumed to be where the highest velocity magnitude is. For the single hole lances the plotting is simple because the jet centreline is a straight line. The jet centreline velocities of one jet in a three-hole lance and the jet of single hole lance is presented in Figure 23. The dimensionless axial distance from the lance is based on the exit radius and dimensionless velocity on the exit velocity of the one-hole lance. It can be seen that one jet of a three-hole lance decays rapidly compared to a jet from a single hole lance of the same flow rate. The dimensionless velocity is plotted against the dimensionless axial distance, which is not the length of the jet in the three-hole lance case. Jet heating due to hot the ambient temperature can be seen in Figure 24, it has a cooling effect on the surface.

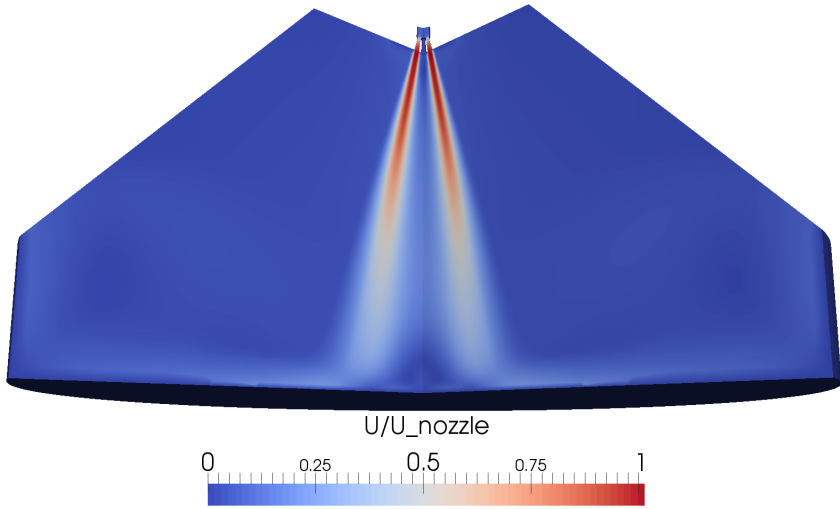


**Fig. 22. Dimensionless jet velocity showing jet bending in a three-hole lance (modified from Paper I © 2013 Trans Tech Publications).**

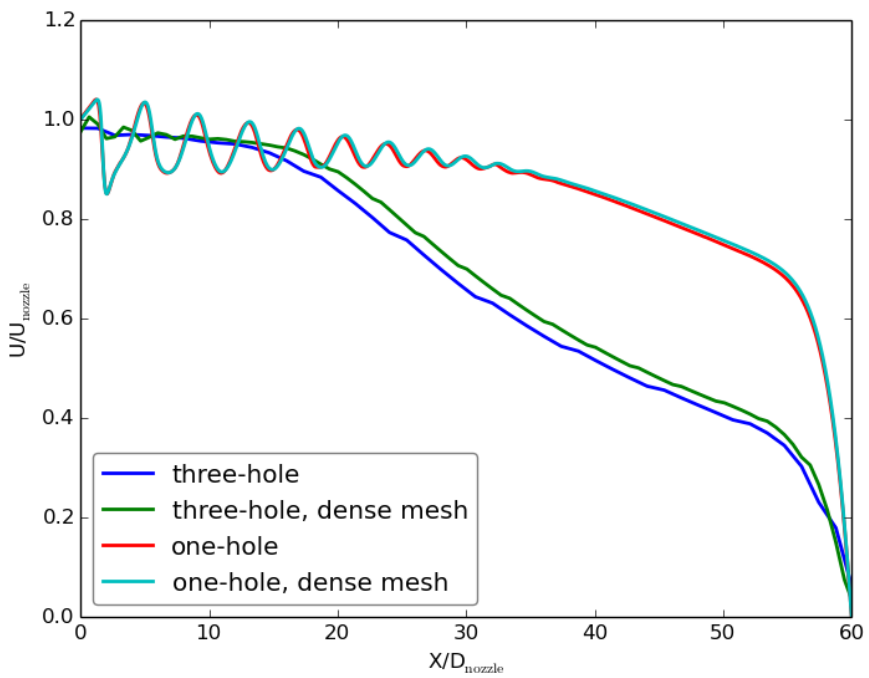


**Fig. 23. Dimensionless jet velocity for one and three-hole lances of same flow rate.**

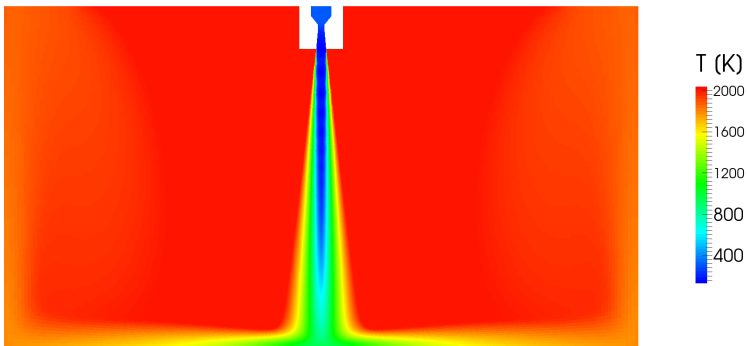


Fig. 24. Temperature of the jet at an ambient temperature of 2000 K, with a one-hole lance.

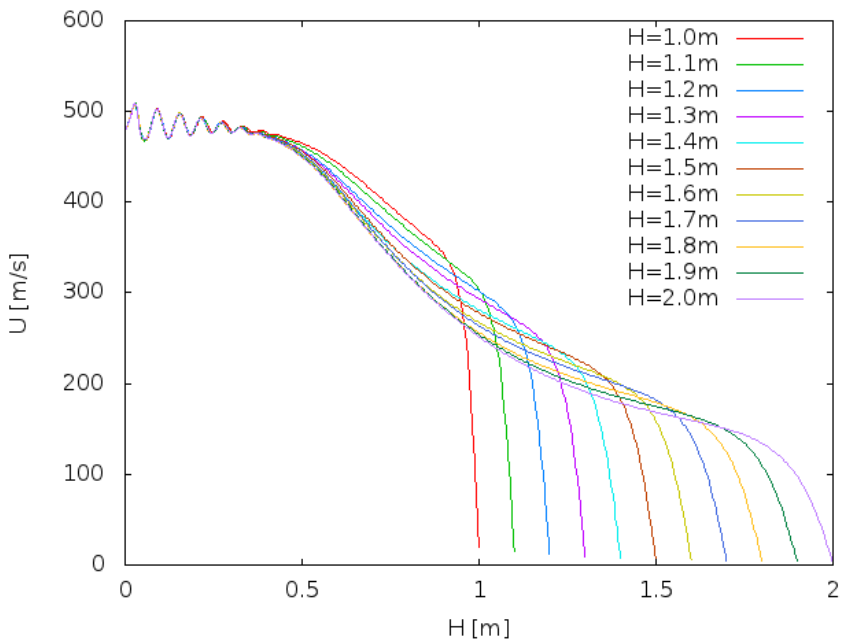
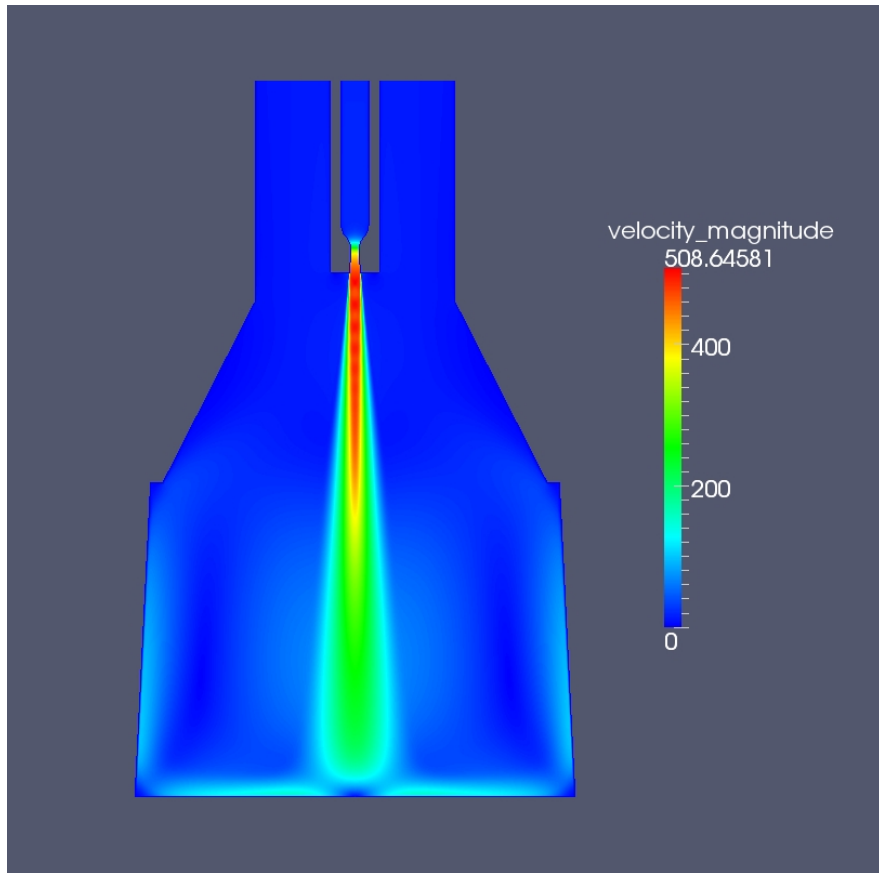


Fig. 25. Lance jet centreline velocities inside the CAS-OB bell (Paper III © 2015 Wiley-VCH).



**Fig. 26.** The CAS-OB lance jet inside the bell, with a lance height of 1.5 m (modified from Paper III © 2015 Wiley-VCH).

The CAS-OB lance jet centreline velocity is presented in Figure 25 at 11 different lance heights. The bell interior space affects the flow so that the velocity after the potential core is higher at a lower lance height. The shape of the jet and the bell geometry is presented in Figure 26, and the lance height is 1.5 m.

#### **4.1.3 Lance heat and mass transfer coefficients**

A comparison of the Nusselt number for one and three-hole lances is presented in Figure 27. The local Nusselt number is plotted as a function of the radial distance from the wall centre, where the lance head points. The figure shows a section through the centre of

one jet of the three, another section in between the jets, the tangentially averaged three jet value and a single nozzle lance curve. When the Nusselt numbers are averaged over the whole surface, the results are close to each other. The one hole lance has a value of  $\bar{Nu}=3380$ , while the three-hole lance has a value of  $\bar{Nu}=3120$ . In a mesh sensitivity test (Figure 23) it was found that the 2D case of one hole lance is not mesh dependent in practical calculations, but the 3D three-hole lance case is limited by computational power. The difference in Nu was found to be about 3% between a 0.8 million cells case and a 5 million cells case. The values of Nu are not exact, but the efficiency of the lances is quite similar.

In practice the deformation of the melt surface and splashing are more significant when using a single-hole lance, which is perhaps the main difference between the lances. In a real process environment, the slag layer protects the steel surface and the slag is removed only in the central region of the jet. The results can be different in terms of the amount of oxygen meeting the steel melt. It could be, that if the flow from multi-hole lance is powerful enough, it would clear a greater area from the slag and would be more efficient. Therefore, the relative efficiency of lances of different types is probably a function of the blowing rate, the lance height, the amount of slag and the converter diameter.

In this case the average Nusselt number over the whole surface was similar for the one-hole and multi-hole lance in the same conditions, but this might not be the case always. However, each different case is possible to predict by means of CFD simulations, and the results can be used in process simulation software that do not include fluid flow simulations.

For the CAS-OB lance the heat transfer was simulated for 11 geometries of different lance heights. The resulting heat transfer coefficients from the lance to the melt surface are given in Figure 28.

When the average heat transfer coefficients are calculated for the whole melt surface inside the bell, the dependence on the lance height is nearly linear in Figure 29. When fitted with a linear equation, the correlation becomes:

$$\alpha_g = -115H_l + 453[W/(m^2K)]. \quad (136)$$

In the same manner the average convection heat transfer coefficient for the bell interior walls as a function of the lance height was determined as

$$\alpha_{bell,in} = -26H_l + 125. \quad (137)$$

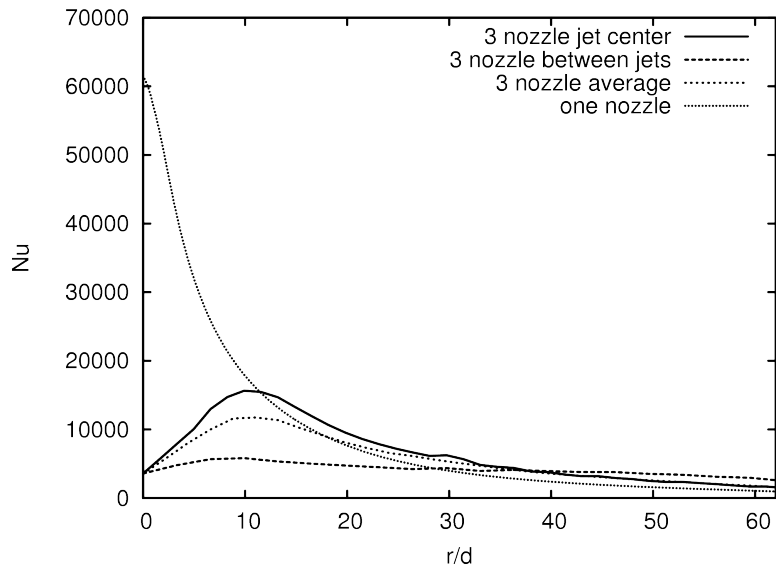


**Fig. 27.** The Nusselt number for a three-hole lance and a single-hole lance (modified from Paper I © 2013 Trans Tech Publications).

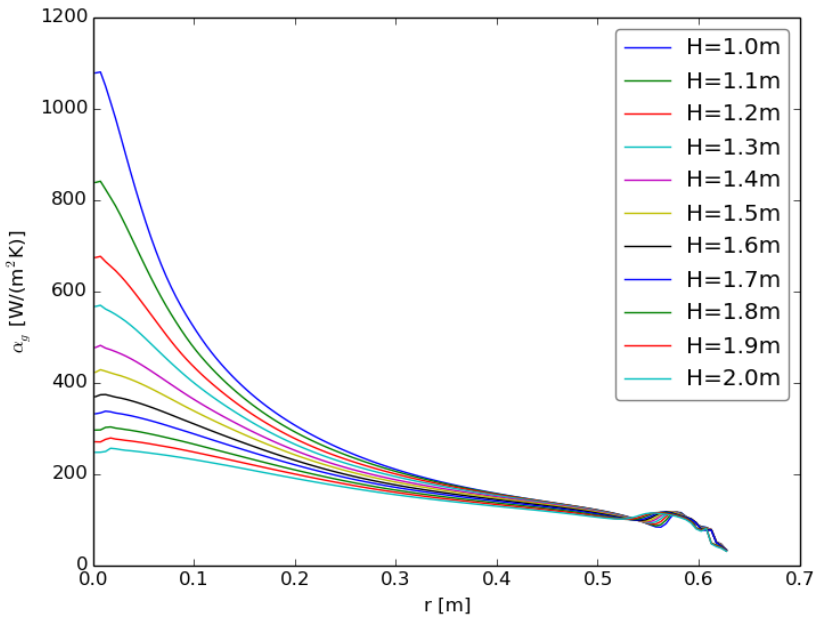


**Fig. 28.** Radial profiles of the heat transfer coefficient at different CAS-OB lance heights.

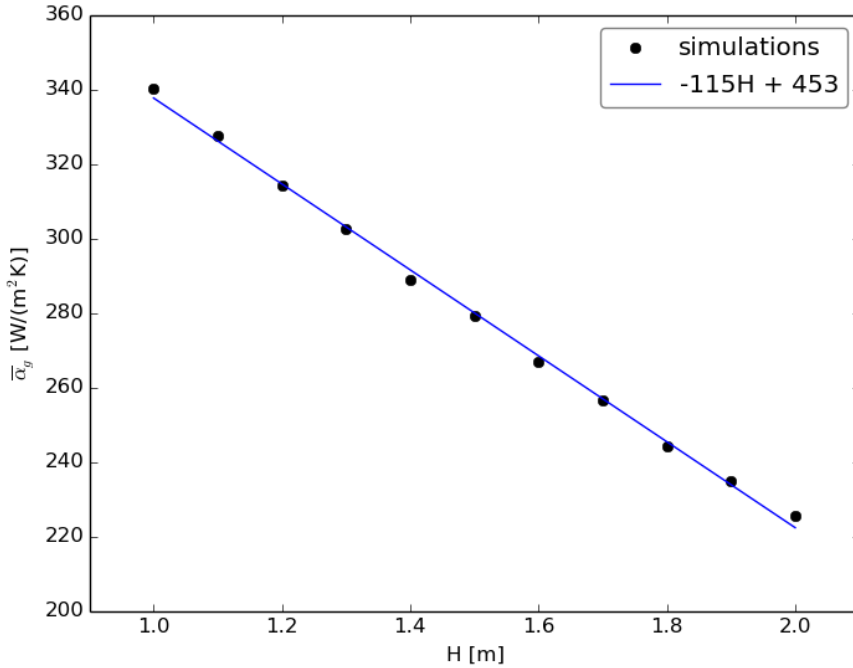


**Fig. 29. Average heat transfer coefficient as a function of the lance height.**

#### **4.1.4 View factors**

Because of the relatively complex geometry of the bell and ladle system, view factors were determined using the Fluent software package. Separate meshes were used for three heights of the bell:

1. A bell submerged in the melt.
2. A bell raised to the measurement position.
3. A bell raised to the normal upper position.

The measurement position of the bell was chosen to give the pyrometer optimal view inside the bell. The view factors are given in Tables 5, 6 and 7.

**Table 5. View factors when the bell is on the melt (Paper IV © 2018 Wiley-VCH).**

To the surface	From the surface					
	Free	Occupied	Bell in	Slag	Ladle	Bell exterior
Free			$A_f/A_{B,in}$			
Occupied			$A_o/A_{B,in}$			
Bell in	1.0000	1.0000				
Slag					0.2201	0.1881
Ladle				0.3464	0.0545	0.3230
Bell exterior				0.2195	0.2398	
Environment				0.4341	0.4857	0.4888

**Table 6. View factors when the bell is at the normal position above the ladle (modified from Paper IV © 2018 Wiley-VCH).**

To the surface	From the surface					
	Open eye	Slag	Ladle	Bell int.	Bell bottom	Bell exterior
Open eye			0.0069	0.0404	0.0682	
Slag			0.2694	0.1424	0.7289	0.0363
Ladle	0.1073	0.2869	0.0967	0.0297	0.1972	0.1302
Bell in	0.4789	0.1204	0.0255	0.7870		
Bell bottom	0.2009	0.1540	0.0393			
Bell exterior		0.0365	0.1261			
Environment	0.2128	0.4022	0.4361	0.0007	0.0057	0.8334

**Table 7. View factors when the bell is at the pyrometer measurement position above the ladle (modified from Paper IV © 2018 Wiley-VCH).**

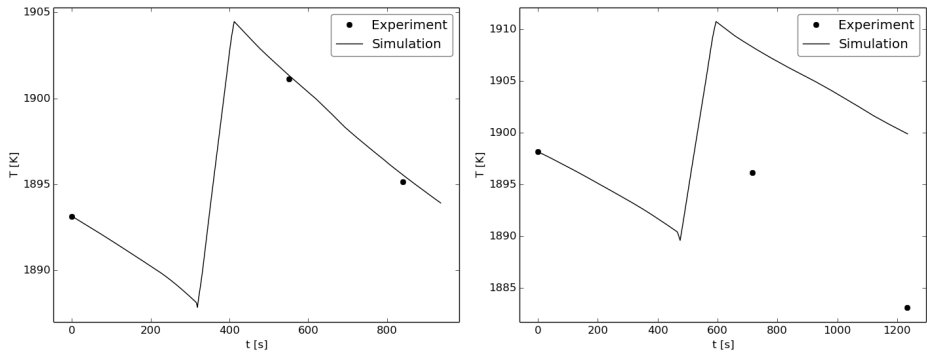
To the surface	From the surface					
	Open eye	Slag	Ladle	Bell int.	Bell bottom	Bell exterior
Open eye			0.0069	0.0159	0.0488	
Slag			0.2694	0.1081	0.4564	0.0092
Ladle	0.1075	0.2870	0.0970	0.05231	0.2682	0.0374
Bell in	0.1815	0.0894	0.0440	0.7870		
Bell bottom	0.1465	0.0967	0.0529			
Bell exterior		0.0092	0.0356			
Environment	0.5645	0.5176	0.4943	0.0368	0.2265	0.9534

## 4.2 CAS-OB heating stage process model

For model validation, the 9 heats that were measured were simulated with the process model. The initial values of the steel and slag masses and composition were set according to the measurements, as well as the melt temperature. Data on the argon, oxygen and aluminium feed was also provided as an input to the model. From these inputs, the model simulated the heating stage of the CAS-OB, together with a cooling period until the end temperature measurement was taken. The simulated and measured values of the compositions and temperatures are given as results.

**Table 8. Temperature measurements and simulation results (modified from Paper IV © 2018 Wiley-VCH).**

Time	Measurement [K]	Simulation [K]	Time	Measurement [K]	Simulation [K]
Heat 2014/1			Heat 2015/1		
before	1870	1870	before	1868	1868
after	1881	1878.7	after	1877	1880.3
end	1867	1866.8	end	1868	1873.2
Heat 2014/2			Heat 2015/2		
before	1893	1893	before	1869	1869
after	1901	1901.3	after	1871	1877.7
end	1895	1895.6	end	1861	1866.5
Heat 2014/3			Heat 2015/3		
before	1884	1884	before	1858	1858
after	1891	1891.9	after	1890	1868.0
end	1872	1884.2	end	1860	1858.1
Heat 2014/4			Heat 2015/4		
before	1876	1876	before	1898	1898
after	1888	1887.2	after	1896	1908.3
end	1873	1876.7	end	1883	1899.9
Heat 2014/5					
before	1886	1886			
after	1898	1893.5			
end	1883	1882.0			
MAE 2014			MAE 2015		
after	1.8		after	11.0	
end	3.5		end	7.3	



(a) Heat 2014/2.

(b) Heat 2015/4.

**Fig. 30. A good and bad example of the match between the simulations and measurements of the steel melt temperature (modified from Paper IV © 2018 Wiley-VCH).**

#### 4.2.1 Temperature

The temperature results are given in Table 8. The example simulation results with measurement points are presented in Figure 30, showing a good match (30a) and a poor match (30b). In the poor match for heat 2015/4, the measured temperature after heating was lower than the starting temperature, which means that either the ladle was very cold, or the start measurement has an error. In the heat 2015/3 the after-heating temperature measurement clearly contains an error. In the case of heat 2015/4, it was found, that the ladle had been empty for an unusually long time before tapping for 461 minutes instead of a normal approximately 100 minutes. In its current state the models does not take this into account, but the initial ladle temperature profile was the same for all the calculated cases. In the future a model for initial ladle temperature could be devised. The cooling rate of the melt, when the heating is not in action, was found to be around 1-1.5 K/min, which is in agreement with literature values of 1-2 K/min (Szekely et al., 1989). The heating rate was about 10 K/min in all cases.

Overall the model predicted the temperature well, if the initial values were correct. There is more difference between the measured and simulated temperatures in the heats of 2015 than in the heats of 2014. One difference between the measurement sets was that in three of the four heats in 2015 the steel was Al-Si-killed, in all others the steel was Al-killed. The only Al-killed steel in 2015 was in heat 2015/4.

The bell interior and ladle exterior simulation results and thermal camera data is presented in Figure 31. The measurement period for the pyrometer data starts after

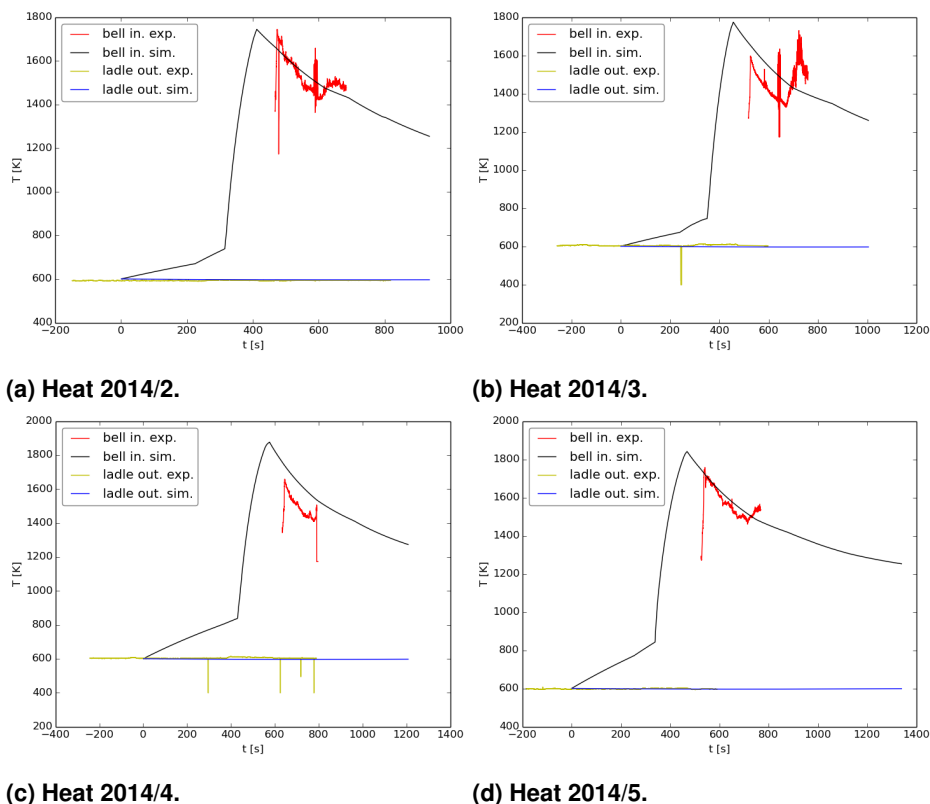
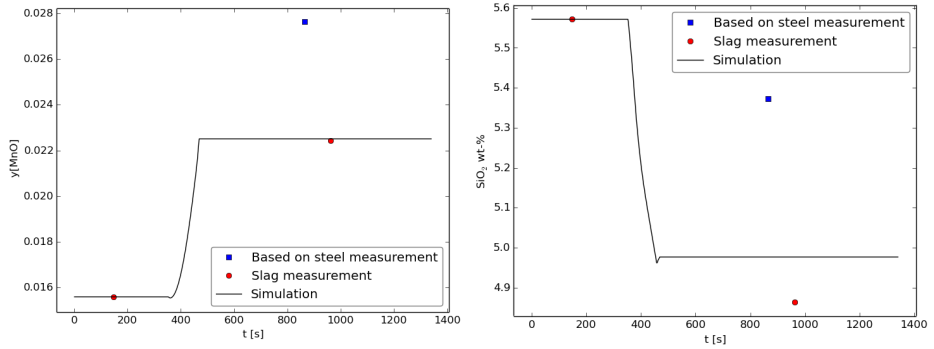


**Fig. 31. Simulations and measurements of the interior bell temperature and exterior ladle temperature (modified from Paper IV © 2018 Wiley-VCH).**

heating, when the bell has risen high enough for a view for the pyrometer. At the end of the pyrometer data argon bottom bubbling starts, causing a rise in the measured temperature as hot gas and dust are fly into the bell. The sharp peaks in the first two heats are due to measurement probe flames.

#### 4.2.2 Chemical composition

The simulation result of the steel composition together with the measurement data is given in Table 9, and the slag data is presented in Table 10. The carbon content of the steel is almost constant as is the silicon in the heats with Al-killed steel, while manganese and aluminium show a larger variation. The largest differences between the simulated and measured values in the steel composition are found in Si and Al,



(a) MnO mass fraction.

(b) SiO<sub>2</sub> mass fraction.

**Fig. 32. Simulation of heat 2014/5 with experimental data from both phases (modified from Paper IV © 2018 Wiley-VCH).**

especially in heats with AlSi-killed steel. In the slag phase the largest error is with FeO for which the model overpredicts the amount of FeO in Al-killed cases and underpredicts it in AlSi-killed cases.

The measurements may have some deviations in the average concentration of the melt or slag due to inhomogeneities of the phases. In the slag phase, the interior bell slag and exterior bell slag are assumed to be fully mixed before the sample is taken after heating. Somewhere there is an error, since the mass is not always conserved in the experiments. The mass lost in one phase is not necessarily found in the other according to the measurements. In the simulations the mass is conserved. An example of this is given in Figure 32, where simulations MnO and SiO<sub>2</sub> are given together with the measured slag phase composition data and the data calculated from the measured steel phase composition.

The model parameters could be fitted to suit the experimental data, for instance the droplet generation rate can be multiplied with an effective constant (Sarkar, Gupta, Basu, & Ballal, 2015; Visuri et al., 2017a). In this model the parameter fitting is retarded by the computational instability, in which some new parameter values in the reaction solver make it necessary to tune the parameters of the iterative solver as well.

**Table 9. Steel measurements and simulation results in wt% (Paper IV © 2018 Wiley-VCH).**

Time	C	Si	Mn	Al	Time	C	Si	Mn	Al
Heat 2014/1					Heat 2015/1				
before	0.034	0.013	0.193	0.034	before	0.05	0.131	1.32	0.031
after	0.034	0.014	0.182	0.036	after	0.05	0.104	1.25	0.04
simulation	0.034	0.010	0.184	0.054	simulation	0.050	0.113	1.263	0.033
Heat 2014/2					Heat 2015/2				
before	0.05	0.009	0.202	0.05	before	0.051	0.135	1.38	0.045
after	0.051	0.009	0.195	0.045	after	0.054	0.119	1.31	0.057
simulation	0.050	0.007	0.194	0.065	simulation	0.051	0.123	1.338	0.060
Heat 2014/3					Heat 2015/3				
before	0.039	0.007	0.195	0.029	before	0.103	0.21	0.704	0.043
after	0.039	0.009	0.183	0.047	after	0.098	0.161	0.598	0.059
simulation	0.039	0.005	0.187	0.044	simulation	0.102	0.188	0.673	0.051
Heat 2014/4					2015/4				
before	0.033	0.011	0.171	0.042	before	0.039	0.008	0.394	0.036
after	0.034	0.011	0.158	0.049	after	0.039	0.007	0.36	0.047
simulation	0.033	0.007	0.160	0.067	simulation	0.039	0.005	0.372	0.057
Heat 2014/5									
before	0.031	0.009	0.169	0.043					
after	0.032	0.01	0.159	0.051					
simulation	0.031	0.007	0.161	0.065					
MAE 2014					MAE 2015				
after	0.001	0.003	0.002	0.015	after	0.002	0.011	0.032	0.007

**Table 10. Slag measurements and simulation results in wt% (Paper IV © 2018 Wiley-VCH).**

Time	Al <sub>2</sub> O <sub>3</sub>	SiO <sub>2</sub>	MnO	FeO	Time	Al <sub>2</sub> O <sub>3</sub>	SiO <sub>2</sub>	MnO	FeO
Heat 2014/1					Heat 2015/1				
before	36.816	5.935	1.711	3.337	before	31.733	13.105	1.506	0.914
after	42.160	5.229	2.544	6.055	after	31.409	13.702	7.768	1.483
simulation	39.775	5.543	2.422	8.864	simulation	34.062	13.814	7.741	1.352
Heat 2014/2					Heat 2015/2				
before	33.942	5.602	1.354	3.632	before	34.692	11.310	1.275	0.522
after	41.225	5.126	2.264	3.508	after	35.129	11.993	7.111	1.511
simulation	38.702	5.052	2.130	7.969	simulation	37.695	11.616	5.499	0.941
Heat 2014/3					Heat 2015/3				
before	32.320	5.478	1.990	6.089	before	36.384	10.521	1.322	1.034
after	41.207	4.458	3.103	6.112	after	38.223	10.179	7.133	10.710
simulation	36.635	4.871	2.586	11.152	simulation	38.267	12.846	4.486	1.465
Heat 2014/4					2015/4				
before	33.813	5.110	1.692	4.154	before	37.924	5.386	3.866	4.457
after	43.560	4.529	2.518	4.217	after	43.681	4.626	6.668	5.110
simulation	39.071	4.690	2.603	10.771	simulation	41.375	4.807	5.329	9.104
Heat 2014/5									
before	30.917	5.572	1.559	5.144					
after	39.777	4.864	2.243	4.366					
simulation	37.572	4.976	2.251	9.124					
MAE 2014					MAE 2015				
after	3.235	0.215	0.173	4.724	after	1.892	0.834	1.406	3.485

## 5 Conclusions

In this work supersonic lance and the CAS-OB heating stage were studied and modelled. The main results of the work are:

1. A turbulence model for a supersonic lance
2. Heat and mass transfer coefficients for CAS-OB by CFD simulations
3. A CAS-OB heating stage process model

Parts of the work were done by means of CFD simulations, where the commercial software package Ansys Fluent was used together with small pieces of C code for user defined functions (UDFs) for user defined tasks. The CAS-OB process model was made using the C++ programming language. When a computational mesh in CFD can contain millions of cells the CAS-OB process model has only a few computational nodes. One result of this work was in showing that CFD can be effectively used to provide input for other modelling software. In the supersonic nozzle modelling, a good match was obtained between the model and experimental data. This is obvious, since the turbulence model parameters were tuned for this purpose. In the CAS-OB process model the same kind of parameter fitting was not done, and it was found that it is not possible. This is because according to the measurements of the steel and slag chemical composition, mass conservation is not always fulfilled. In the model the mass is conserved. Considering the uncertainties in chemical composition and mass measurements, the results show a reasonable match between the simulations and the measurements. The most important result of the model, the steel temperature, shows better agreement with the measurements than the chemical composition.

The lance modelling results are directly usable in CAS-OB models and the methods can be applied to any process involving a top lance. The CAS-OB heating stage process model can be used in process development and optimization, and as a research tool in studying process mechanisms.

### Recommendations for future work

Supersonic lance theory and modelling are both quite well known, but supersonic jet impingement is not. As there is no experimental data on the supersonic jet impingement, full scale heat transfer experiments would be very useful. On the CFD modelling side,

the turbulence models for jet impingement are not perfect yet and more research is needed.

One major topic in the CAS-OB process model was getting the reaction system to reach a mass transfer limited equilibrium at the reaction surfaces. This was not monitored in the initial model, and later it turned out to be a major challenge in the calculation process. In future work it would be useful to further study what size  $k_f$  values are actually necessary for the system to give reliable results. If very large values are not needed the system would be easier to solve. With a faster solution, the models could be used for online purposes at steel plants. Another possibility is to develop the stability of the solution method. For instance, the currently used scheme to slowly increase the  $k_f$  values could be replaced with another way to approach the equilibrium state.

The law of mass action based system used in this work iterates the solution with reaction rates and the mass transfer rates simultaneously, providing an accurate solution for mass conservation. The gain in accuracy is paid for with a complicated system and sometimes poor convergence. The Gibbs energy minimization systems usually use a reaction zone, which is first set to an equilibrium composition and mass transfer is applied separately, yielding some errors but with easier calculation. Different methods should be studied by applying them to the same problems and then comparing accuracy, computational effort and reliability of the methods.

The last development topic concerns the industrial measurements. The mass conservation problem in the composition measurement data and errors in the temperature measurements should be carefully studied. Reasons for inaccurate measurements could be:

- Inhomogeneous concentration/temperature
- Measurement errors
- Inaccurate equipment/methods

Inhomogeneity is a probable cause of deviation in concentration analysis, and it could also affect the temperature measurement taken after heating. A greater number of experiments would be helpful to create reliable statistics on the phenomena studied. The number of measurements is limited by the disturbance and delay caused to the process, therefore new measurement methods should be developed. Finally the developed computational models should be used to make the existing processes better and to develop new ones.

## References

- Alam, M., Naser, J., & Brooks, G. (2010). Computational fluid dynamics simulation of supersonic oxygen jet behavior at steelmaking temperature. *Metallurgical and Materials Transactions B*, 41(3), 636–645.
- Allemand, B., Bruchet, P., Champinot, C., Melen, S., & Porzucek, F. (2001). Theoretical and experimental study of supersonic oxygen jets. Industrial application in EAF. *Revue de Métallurgie*, 98(6), 571–587.
- Andersson, N., Tilliander, A., Jonsson, L., & Jönsson, P. (2013). Fundamental decarburisation model of AOD process. *Ironmaking & Steelmaking*, 40(5), 390–397.
- Ansys Inc. (2009). *Ansys Fluent 12.0 theory guide*.
- Audebert, S., Gugliermina, P., Reboul, J.-P., & Sauermann, M. (1989). The CAS-OB Process in the Steelshop of Fos sur Mer—Conception and First Operating Results. *Scaninject V. Part I*, 709–722.
- Bale, C. W., & Pelton, A. D. (1990). The unified interaction parameter formalism: Thermodynamic consistency and applications. *Metallurgical Transactions A*, 21(7), 1997–2002.
- Ban-Ya, S. (1993). Mathematical expression of slag-metal reactions in steelmaking process by quadratic formalism based on the regular solution model. *ISIJ International*, 33(1), 2–11.
- Bhattacharya, T., Zhan, L., & Chukwulebe, B. (2015). A numerical test bench for supersonic oxygen nozzles and its application to the BOF process. *Proceedings of the AISTech*, 1149–1158.
- Bird, R. B., Stewart, W. E., & Lightfoot, E. N. (1960). *Transport phenomena*. New York, USA: John Wiley & Sons, Inc.
- Brooks, G., Pan, Y., Subagyo, & Coley, K. (2005). Modeling of trajectory and residence time of metal droplets in slag-metal-gas emulsions in oxygen steelmaking. *Metallurgical and Materials Transactions B*, 36(4), 525–535.
- Chatterjee, A. (1972). On some aspects of supersonic jets of interest in LD steelmaking. *Iron and Steel*, 45(6), 627–634.
- Chatterjee, A., & Bradshaw, A. (1973). The influence of gas phase resistance on mass transfer to a liquid metal. *Metallurgical Transactions*, 4(5), 1359–1364.

- Chatterjee, A., Marique, C., & Nilles, P. (1984). Overview of present status of oxygen steelmaking and its expected future trends. *Ironmaking & Steelmaking*, 11(3), 117–131.
- Chatterjee, A., Wakelin, D., & Bradshaw, A. (1972). Mass transfer from an oxygen jet to liquid silver. *Metallurgical Transactions*, 3(12), 3167–3172.
- Deo, B., & Boom, R. (1993). *Fundamentals of steelmaking metallurgy*. New York, NY, USA: Prentice-Hall.
- Dogan, N., Brooks, G. A., & Rhamdhani, M. A. (2011a). Comprehensive model of oxygen steelmaking part 1: Model development and validation. *ISIJ International*, 51(7), 1086–1092. doi: 10.2355/isijinternational.51.1086
- Dogan, N., Brooks, G. A., & Rhamdhani, M. A. (2011b). Comprehensive model of oxygen steelmaking part 3: decarburization in impact zone. *ISIJ International*, 51(7), 1102–1109.
- Douglas, J., Gasiorek, J., & Swaffield, J. (1986). *Fluid mechanics*. Harlow, Essex, England: Prentice-Hall.
- Eggers, J. M. (1966). Velocity profiles and eddy viscosity distributions downstream of a Mach 2.22 nozzle exhausting to quiescent air. *NASA technical note, NASA TN D-3601*.
- Eriksson, G. (1971). Thermodynamic study of high temperature equilibria. *Acta Chemica Scandinavica*, 25(7), 2651–2658.
- Ersson, M., Höglund, L., Tilliander, A., Jonsson, L., & Jönsson, P. (2008). Dynamic coupling of computational fluid dynamics and thermodynamics software: applied on a top blown converter. *ISIJ International*, 48(2), 147–153.
- Ersson, M., Tilliander, A., Jonsson, L., & Jönsson, P. (2008). A mathematical model of an impinging air jet on a water surface. *ISIJ International*, 48(4), 377–384.
- Ferziger, J. H., & Peric, M. (1996). *Computational methods for fluid dynamics*. Berlin, Germany: Springer-Verlag.
- Fredman, T., & Saxen, H. (1998). Model for temperature profile estimation in the refractory of a metallurgical ladle. *Metallurgical and Materials Transactions B*, 29(3), 651–659.
- Fredman, T. P., Torrkulla, J., & Saxen, H. (1999). Two-dimensional dynamic simulation of the thermal state of ladles. *Metallurgical and Materials Transactions B*, 30(2), 323–330.
- Geiger, G. H., & Poirier, D. R. (1973). *Transport phenomena in metallurgy*. Reading, Mass. USA.: Addison-Wesley Publishing Co.

- Ha, C.-S., & Park, J. (2008). Start-up and some experience of CAS-OB at POSCO. *Archives of Metallurgy and Materials*, 53(2), 637–642.
- Higbie, R. (1935). The rate of absorption of a pure gas into a still liquid during short periods of exposure. *Transactions of the American Institute of Chemical Engineers*, 31(3), 365–389.
- Incropera, F. P., & De Witt, D. P. (1985). *Fundamentals of heat and mass transfer*. New York, USA: John Wiley & Sons.
- Jalkanen, H. (2006). Experiences in physicochemical modelling of oxygen converter process(BOF). In *Sohn international symposium; advanced processing of metals and materials volume 2: Thermo and physicochemical principles: Iron and steel making* (Vol. 2, pp. 541–554).
- Järvinen, M., Visuri, V.-V., Heikkinen, E.-P., Kärnä, A., Sulasalmi, P., De Blasio, C., & Fabritius, T. (2016). Law of mass action based kinetic approach for the modelling of parallel mass transfer limited reactions: Application to metallurgical systems. *ISIJ International*, 56(9), 1543–1552.
- Järvinen, M. P., Pisilä, S., Kärnä, A., Ikäheimonen, T., Kupari, P., & Fabritius, T. (2011). Fundamental mathematical model for AOD process. Part I: Derivation of the model. *Steel Research International*, 82(6), 638–649.
- Kataoka, H., & Miyauchi, T. (1969). Gas absorption into the free liquid surface of water tunnel in turbulent region. *Chemical Engineering*, 33(2), 181-186.
- Kawai, Y., Shiraishi, Y., Kyōkai, N. T., & 140th Committee, N. G. S. (1988). *Handbook of physico-chemical properties at high temperatures*. Iron and Steel Institute of Japan.
- Kirkaldy, J. S., & Ward, R. G. (1964). *Aspects of modern ferrous metallurgy*. Toronto, Canada: University of Toronto Press.
- Koria, S. C. (1988). Nozzle design in impinging jet steelmaking processes. *Steel Research International*, 59(3), 104–109.
- Koria, S. C., & Lange, K. W. (1984). An experimental study on the behaviour of an underexpanded supersonic gas jet. *Steel Research International*, 55(9), 427–432.
- Koria, S. C., & Lange, K. W. (1987). Penetrability of impinging gas jets in molten steel bath. *Steel Research International*, 58(9), 421–426.
- Koukkari, P., & Pajarre, R. (2011). A Gibbs energy minimization method for constrained and partial equilibria. *Pure and Applied Chemistry*, 83(6), 1243–1254.
- Kulju, T., Ollila, S., Keiski, R. L., & Muurinen, E. (2013). Three phase CFD-simulation of CAS-OB ladle. *Materials Science Forum*, 762, 248–252.

- Kulju, T., Ollila, S., Keiski, R. L., & Muurinen, E. (2015). Validation of three-phase CAS-OB CFD-model. *IFAC-PapersOnLine*, 48(17), 1 - 5. doi: <https://doi.org/10.1016/j.ifacol.2015.10.067>
- Kusunoki, S., Nishihara, R., Kato, K., Sakagami, H., Hirashima, S., & Fukunaga, N. (2013). Development of Steelmaking Processes for Producing Various High-Quality Steel Grades at Yawata Works. *Nippon steel technical report*, 104.
- Laakkonen, M., Alopaeus, V., & Aittamaa, J. (2006). Validation of bubble breakage, coalescence and mass transfer models for gas-liquid dispersion in agitated vessel. *Chemical Engineering Science*, 61(1), 218–228.
- Lauder, B. E., & Spalding, D. B. (1974). The numerical computation of turbulent flows. *Computer Methods in Applied Mechanics and Engineering*, 3(2), 269–289.
- Lee, M., O'Rourke, S., & Molloy, N. (2002). Fluid flow and surface waves in the BOF. *Iron & Steelmaker*, 29(10), 56–65.
- Li, M., Li, Q., Kuang, S., & Zou, Z. (2016). Transferring characteristics of momentum/energy during oxygen jetting into the molten bath in BOFs: A computational exploration. *Steel Research International*, 87(3), 288–300.
- Li, Q., Li, M., Kuang, S., & Zou, Z. (2014). Computational study on the behaviours of supersonic jets and their impingement onto molten liquid free surface in BOF steelmaking. *Canadian Metallurgical Quarterly*, 53(3), 340–351.
- Li, Q., Li, M., Kuang, S., & Zou, Z. (2015). Numerical simulation of the interaction between supersonic oxygen jets and molten slag–metal bath in steelmaking BOF process. *Metallurgical and Materials Transactions B*, 46(3), 1494–1509.
- Li, Y., Lou, W., & Zhu, M. (2012). Numerical simulation of gas and liquid flow in steelmaking converter with top and bottom combined blowing. *Ironmaking & Steelmaking*, 40(7), 505–514.
- Linstrom, P., & Mallard, W. (Eds.). (2017). *NIST chemistry webbook*. National Institute of Standards and Technology.
- Lohe, H. (1966). Zum wärme-und stoffaustausch beim senkrechten aufblasen von gasstrahlen auf flüssigkeitsoberflächen. *Chemie Ingenieur Technik*, 38(3), 309–314.
- Lohe, H. (1967). Wärme-und stofftransport beim aufblasen von gasstrahlen auf flüssigkeiten. *Fortschritt Berichte VDI Zeitschrift*, 3(15), 1–59.
- Ma, W.-J., Bao, Y.-P., Zhao, L.-H., & Wang, M. (2014). Physical modelling and industrial trials of CAS-OB refining process for low carbon aluminium killed steels. *Ironmaking & Steelmaking*, 41(8), 607–610.

- Mazumdar, D., & Guthrie, R. (1995). On the numerical computation of turbulent fluid flow in CAS steelmaking operations. *Applied Mathematical Modelling*, 19(9), 519–524.
- Menter, F. R. (1994). Two-equation eddy-viscosity turbulence models for engineering applications. *AIAA Journal*, 32(8), 1598–1605.
- Nilsson, L., Andersson, K., & Lindquist, K. (1996). The CAS-OB process in the steelshop at SSAB Tunnpå AB, Luleå works. *Scandinavian Journal of Metallurgy*, 25(2), 73–79.
- Odenhal, H.-J., Falkenreck, U., & Schlüter, J. (2006). CFD simulation of multiphase melt flows in steelmaking converters. In *Eccomas cfd 2006: Proceedings of the european conference on computational fluid dynamics, egmond aan zee, the netherlands, september 5-8, 2006*.
- Oeters, F. (1994). *Metallurgy of steelmaking*. Düsseldorf, Germany: Verlag Stahleisen.
- Ollila, S., Syrjänen, A., & Robey, R. (2011). Commissioning and initial results from new twin CAS-OB plant at Ruukki, Raahe Steel Works. In *The 6th european oxygen steelmaking conference* (pp. 170–183).
- Outotec. (2015). *HSC Chemistry 8*.
- Pan, Y., Guo, D., Ma, J., Wang, W., Tang, F., & Li, C. (1994). Mixing time and fluid flow pattern of composition adjustment by sealed argon bubbling with ladles of large height/diameter ratio. *ISIJ International*, 34(10), 794–801.
- Pelton, A. D., & Bale, C. W. (1986). A modified interaction parameter formalism for non-dilute solutions. *Metallurgical Transactions A*, 17(7), 1211–1215.
- Pisilä, S. E., Järvinen, M. P., Kärnä, A., Ikäheimonen, T., Fabritius, T., & Kupari, P. (2011). Fundamental mathematical model for AOD process. Part II: Model validation. *Steel Research International*, 82(6), 650–657.
- Pope, S. B. (2000). *Turbulent flows*. Cambridge, England: Cambridge University Press.
- Rout, B. K., Brooks, G., Subagyo, Rhamdhani, M. A., & Li, Z. (2016). Modeling of droplet generation in a top blowing steelmaking process. *Metallurgical and Materials Transactions B*, 47(6), 3350–3361.
- Sarkar, R., Gupta, P., Basu, S., & Ballal, N. B. (2015). Dynamic modeling of LD converter steelmaking: Reaction modeling using Gibbs' free energy minimization. *Metallurgical and Materials Transactions B*, 46(2), 961–976.
- Shaw, C. T. (1992). *Using computational fluid dynamics*. Hemel Hempstead, England: Prentice Hall.
- Shih, T.-H., Liou, W. W., Shabbir, A., Yang, Z., & Zhu, J. (1995). A new k-ε eddy

- viscosity model for high reynolds number turbulent flows. *Computers & Fluids*, 24(3), 227–238.
- Shoemaker, C. J. (1965). Performance of seven semicircular lift-producing nozzles. *NASA Technical Note, NASA TN D-2731*.
- Smith, G. (1966). Multiple jet oxygen lances—Theoretical analysis and correlation with practice. *JOM*, 18(7), 846–851.
- Spalart, P., & Allmaras, S. (1992). A one-equation turbulence model for aerodynamic flows. In *30th aerospace sciences meeting and exhibit*.
- Stolte, G. (2007). *Secondary metallurgy*. Düsseldorf, Germany: Verlag Stahleisen.
- Subagyo, Brooks, G. A., Coley, K. S., & Irons, G. A. (2003). Generation of droplets in slag-metal emulsions through top gas blowing. *ISIJ International*, 43(7), 983-989.
- Sulasalmi, P., Kärnä, A., Fabritius, T., & Savolainen, J. (2009). CFD Model for Emulsification of Slag into the Steel. *ISIJ International*, 49(11), 1661–1667.
- Sulasalmi, P., Visuri, V.-V., & Fabritius, T. (2013). Effect of interfacial tension on the emulsification of slag -considerations on the CFD modelling of dispersion. *Materials Science Forum*, 762, 242–247.
- Sulasalmi, P., Visuri, V.-V., Kärnä, A., & Fabritius, T. (2015). Simulation of the effect of steel flow velocity on slag droplet distribution and interfacial area between steel and slag. *Steel Research International*, 86(3), 212–222.
- Sulasalmi, P., Visuri, V.-V., Kärnä, A., Järvinen, M., Ollila, S., & Fabritius, T. (2016). A mathematical model for the reduction stage of the CAS-OB process. *Metallurgical and Materials Transactions B*, 47(6), 3544–3556.
- Sumi, I., Kishimoto, Y., Kikuchi, Y., & Igarashi, H. (2006). Effect of high-temperature field on supersonic oxygen jet behavior. *ISIJ International*, 46(9), 1312–1317.
- Szekely, J., Carlsson, G., & Helle, L. (1989). *Ladle metallurgy*. New York, USA: Springer-Verlag.
- Venturini, G., & Goldschmit, M. B. (2007). Gas-liquid reaction model in gas-stirred systems: Part 1. Numerical model. *Metallurgical and Materials Transactions B*, 38(3), 461–475.
- Versteeg, H. K., & Malalasekera, W. (2007). *An introduction to computational fluid dynamics: The finite volume method*. Harlow, England: Pearson Education.
- Visuri, V.-V., Järvinen, M., Kärnä, A., Sulasalmi, P., Heikkinen, E.-P., Kupari, P., & Fabritius, T. (2017a). A mathematical model for reactions during top-blowing in the AOD process: Derivation of the model. *Metallurgical and Materials*

- Transactions B*, 48(3), 1850–1867.
- Visuri, V.-V., Järvinen, M., Kärnä, A., Sulasalmi, P., Heikkinen, E.-P., Kupari, P., & Fabritius, T. (2017b). A mathematical model for reactions during top-blowing in the AOD process: Validation and results. *Metallurgical and Materials Transactions B*, 48(3), 1868–1884.
- Wakelin, D. H. (1966). *The interaction between gas jets and the surfaces of liquids, including molten metals* (Unpublished doctoral dissertation). University of London.
- Wang, H.-M., Li, G.-R., Dai, Q.-X., Li, B., Zhang, X.-J., & Shi, G.-M. (2007). CAS-OB refining: slag modification with  $B_2O_3$ -CaO and  $CaF_2$ -CaO. *Ironmaking & Steelmaking*, 34(4), 350–353.
- Wang, W., Yuan, Z., Matsuura, H., Zhao, H., Dai, C., & Tsukihashi, F. (2010). Three-dimensional compressible flow simulation of top-blown multiple jets in converter. *ISIJ International*, 50(4), 491–500.
- Wei, J.-H., & Zhu, D.-P. (2002). Mathematical modeling of the argon-oxygen decarburization refining process of stainless steel: Part I. Mathematical model of the process. *Metallurgical and Materials Transactions B*, 33(1), 111–119.
- Wilcox, D. C. (1998). *Turbulence modeling for CFD, 2nd ed.* La Canada, USA: DCW Industries Inc.
- Xu, Y., Ersson, M., & Jönsson, P. G. (2015). A mathematical modeling study of bubble formations in a molten steel bath. *Metallurgical and Materials Transactions B*, 46(6), 2628–2638.



## Original publications

- I Kärnä, A., Järvinen, M., & Fabritius, T. (2013). Supersonic lance mass transfer modelling. *Materials Science Forum*, 762, 686-690.
- II Järvinen, M., Kärnä, A., Visuri, V.-V., Sulasalmi, P., Heikkinen, E.-P., Pääskylä, K., De Blasio, C., Ollila, S., & Fabritius, T. (2014). A novel approach for numerical modeling of the CAS-OB process: Process model for the heat-up stage. *ISIJ International*, 54(10), 2263-2272.
- III Kärnä, A., Järvinen, M. P., & Fabritius, T. (2015). CFD modeling of a supersonic top blown lance in a CAS-OB process – development of gas heat and mass transfer correlation. *Steel Research International*, 86(11), 1370–1378.
- IV Kärnä, A., Järvinen, M., Sulasalmi, P., Visuri, V.-V., Ollila, S., & Fabritius, T. (2018). An improved model for the heat-up stage of the CAS-OB process: Development and validation. *Steel Research International*, 89(10). doi: 10.1002/srin.201800141

*Reprinted with permission from* Trans Tech Publications (I), Iron and Steel Institute of Japan (II) and Wiley-VCH (III and IV).

*Original publications are not included in the electronic version of the dissertation.*



669. Anttila, Severi (2018) Influence of minor elements on some weldability issues of intermediate purity stabilized ferritic stainless steels
670. Hartmann, Robert (2018) Flotation using cellulose-based chemicals
671. Porambage, Pawani (2018) Lightweight authentication and key management of wireless sensor networks for Internet of things
672. Bibikova, Olga (2018) Plasmon-resonant gold nanoparticles for bioimaging and sensing applications
673. Venkatraman, Ganesh (2018) Traffic aware resource allocation for multi-antenna OFDM systems
674. Isokangas, Elina (2018) Quantifying the groundwater dependence of boreal ecosystems using environmental tracers
675. Tervasmäki, Petri (2018) Reaction and mass transfer kinetics in multiphase bioreactors : experimental and modelling studies
676. Leinonen, Markus (2018) Distributed compressed data gathering in wireless sensor networks
677. He, Jiguang (2018) Performance of MIMO and non-orthogonal transmission in Lossy Forward relay networks
678. Matinmikko-Blue, Marja (2018) Stakeholder analysis for the development of sharing-based spectrum governance models for mobile communications
679. Paaso, Henna (2018) Direction of arrival estimation algorithms for leaky-wave antennas and antenna arrays
680. Pap, Nora (2018) Value-added processing of blackcurrants : Use of membrane technologies for clarification and concentration of blackcurrant juice and extraction of anthocyanins from blackcurrant marc
681. Tolvanen, Jarkko (2018) Novel sensor and switch applications for flexible and stretchable electronic materials
682. Alatarvas, Tuomas (2018) Evolution of inclusion population in calcium treated ultra-high strength steels : Novel applications of sample data treatment
683. Tomperi, Jani (2018) Predicting the treated wastewater quality utilizing optical monitoring of the activated sludge process
684. Fazel Modares, Nasim (2018) The role of climate and land use change in Lake Urmia desiccation

S E R I E S E D I T O R S

**A**  
**SCIENTIAE RERUM NATURALIUM**  
*University Lecturer Tuomo Glumoff*

**B**  
**HUMANIORA**  
*University Lecturer Santeri Palviainen*

**C**  
**TECHNICA**  
*Postdoctoral research fellow Sanna Taskila*

**D**  
**MEDICA**  
*Professor Olli Vuolteenaho*

**E**  
**SCIENTIAE RERUM SOCIALIUM**  
*University Lecturer Veli-Matti Ulvinen*

**E**  
**SCRIPTA ACADEMICA**  
*Planning Director Pertti Tikkanen*

**G**  
**OECONOMICA**  
*Professor Jari Juga*

**H**  
**ARCHITECTONICA**  
*University Lecturer Anu Soikkeli*

**EDITOR IN CHIEF**  
*Professor Olli Vuolteenaho*

**PUBLICATIONS EDITOR**  
*Publications Editor Kirsti Nurkkala*

